Submerged Discharges in Liquids for Nanoobject Synthesis: Expectations and Capabilities

T. Belmonte, A V Nominé, C. Noël, T. Gries, Alexandre Nominé,, V. Milichko, Mohammed Belmahi, M Y Awaji

▶ **To cite this version:**

T. Belmonte, A V Nominé, C. Noël, T. Gries, Alexandre Nominé,, et al.. Submerged Discharges in Liquids for Nanoobject Synthesis: Expectations and Capabilities. Plasma Chemistry and Plasma Processing, 2023, Special Issue: ISPC25, 10.1007/s11090-023-10349-4 . hal-04156074

HAL Id: hal-04156074

https://hal.univ-lorraine.fr/hal-04156074

Submitted on 7 Jul 2023

HAL is a multi-disciplinary open access archive for the deposit and dissemination of scientific research documents, whether they are published or not. The documents may come from teaching and research institutions in France or abroad, or from public or private research centers.

L'archive ouverte pluridisciplinaire **HAL**, est destinée au dépôt et à la diffusion de documents scientifiques de niveau recherche, publiés ou non, émanant des établissements d'enseignement et de recherche français ou étrangers, des laboratoires publics ou privés.

Submerged discharges in liquids for nanoobject synthesis: expectations and capabilities

T. Belmonte[1,*], A. V. Nominé[1], C. Noël[1], T. Gries[1], A. Nominé[1], V. Milichko[1,2], M. Belmahi[1], M. Y. Awaji[1]

[1] *University of Lorraine, CNRS, IJL, F-54000 Nancy, France*
[2] *Department of Nanophotonics and Metamaterials, ITMO University, St. Petersburg, 197101, Russia*
** Corresponding author: thierry.belmonte@univ-lorraine.fr*

Keywords

Solution plasma; glow discharge electrolysis; submerged discharges; nanoobjects; review

Abstract

Electrical discharges in liquids are used to synthesize and process nanoobjects with breakthrough achievements that lead to high expectations in the field. As plasmas are non-equilibrium media, the possibility to access novel compositions, shapes, structures, etc. is often put forward as major argument to promote these processes. Two main classes of processes are considered in this review: the so-called "solution plasma" and glow-discharge electrolysis. The influence of the main parameters controlling the selected processes is discussed. Applications are also presented together with expectations on breakthrough achievements awaited for these processes.

Introduction

It is always interesting to question one's practices and to put the known possibilities of certain processes into perspective with those provided by their competitors. By combining discharges and liquids, it is possible to synthesize original nanoobjects and process them, with the significant advantage of being able to use highly non-equilibrium media.

The multiplication of recent reviews on this subject [1-14] demonstrates the current craze for these approaches, which offer interesting prospects due to their specificities. There are many ways to synthesize or functionalize nanomaterials by discharges, using processes that can be classified as depicted in **Fig. 1**: sputtering onto liquids, spray in plasma, plasma-assisted electrochemistry, and discharges in liquids.

Following Prasad *et al.* [7], liquid-phase production without plasma assistance can be made by six main techniques, namely sol-gel processing, microemulsions, hydrothermal, sonochemical, chemical coprecipitation, and electrochemical methods. All these processes require the presence of a stabilizing agent to prevent aggregation of the resultant nanoparticles, but also many steps like stepwise unit operations of heating, addition of reactants, cooling-down, and removal of supernatant after centrifugation and redispersion.

Jendrzej *et al*. [15] showed in 2017 that laser-based synthesis is more economical than wet-chemical reduction if productivity exceeds 550 mg h^{-1}. Even though this conclusion does not include arguments about key features of nanoparticles, like their shapes, size distributions or compositions, it demonstrates that the economic viability of a process is strongly dependent on the number of processing steps needed to produce the final colloidal solution rather than its energetic cost. This latter parameter, for either process in the given example, is only 1%, and then negligible as labor (55%), investment (12%) and materials (32%) represent 99% of the overall cost of a produced batch. The argument about energy, even though it is perfectly grounded, sounds surprisingly outdated in the world context we know today, putting pulsed processes on par with continuous processes.

As explained by Amans *et al*. [16], laser processes in liquids based on ablation, melting, fragmentation and photoreduction/oxidation offer different routes to obtain colloids with controlled nanoparticle sizes. Laser generation of nanoparticles in liquids may be deemed mature enough for industrial outlets of colloid production. Plasma-based processes in liquids offer many similarities with their laser counterparts and like them, can challenge chemical routes: they offer extreme conditions achievable with non-equilibrium processes and, as such, they generate huge gradients that drive the formation of a whole zoology of nanoobjects. In the case of water splitting, for instance, the size of a cocatalyst deposited onto a photocatalyst can significantly affect the quantum efficiency (by one order of magnitude if it only varies from 2.3 to 5.2 nm, for instance) [17].

However, the wizardry of chemists always goes far beyond our highest expectations. In a seminal work on high entropy alloys, Yao *et al*. [18] presented a general route for alloying up to eight elements into single-phase solid-solution nanoparticles with possible control of size distributions. Nanoparticles produced by these methods deviate from the phase-separated thermodynamic equilibrium structures, as shown in the work of Chen *et al*. [19]. However, this approach allows for independent control of both composition and size, and the formation of phase-separated states can be designed as needed, resulting in libraries consisting of every combination of several (up to five) metallic elements.

In this review, we propose a review of works mainly published after 2018 on electrical discharges submerged in liquids, completed by former results when necessary. These processes (class of processes 1d in **Fig. 1**) are used for nanoobjects synthesis as a basis for comparison with their competitors.

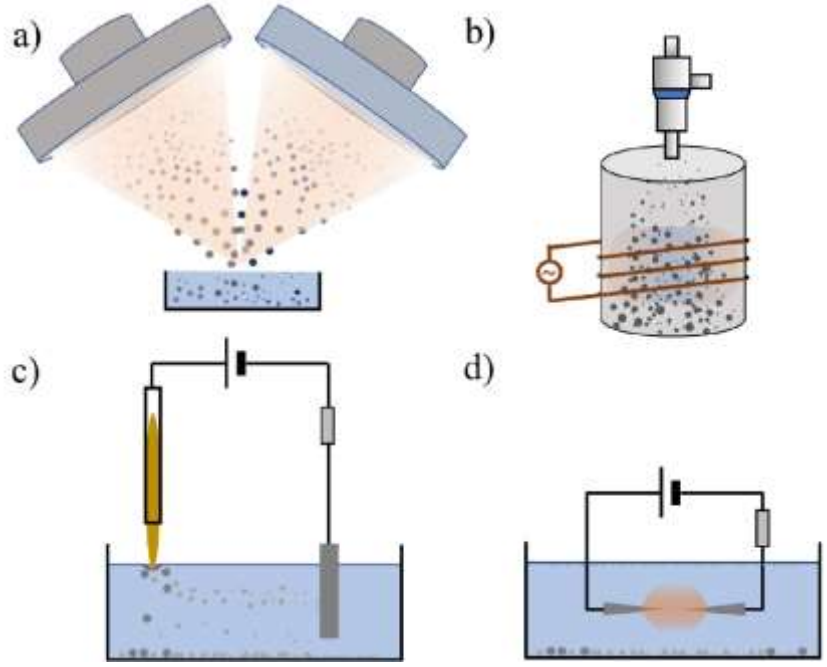

Fig. 1 Main classes of processes involving electrical discharges and liquids: a) sputtering onto liquids, b) spray in plasma, c) plasma-assisted electrochemistry, d) submerged discharges in liquids.

The main advantages of submerged discharges in liquids are taken from [20-22]: (1) a one-step process; (2) an ambient reaction environment; (3) a straightforward and easy setup; (4) a cost-effective production; (5) possible large-scale synthesis quantities; (6) an eco-friendly fabrication; and (7) high control on nanoparticle characteristics (size, shape, composition, etc.)

Different criteria are evaluated, including mastering of size distributions, control over compositions, access to non-equilibrium phases, structure design capabilities, solution stability, and energy cost. After a short description of the classes of processes and the main strategies adopted to synthesize nanoobjects, the

capabilities and limitations of the described processes through the influence of the main parameters dealing with liquid characteristics, process conditions and time, are exposed. Before concluding, expectations are presented together with the applications considered by the researchers.

Classes of processes

Numerous processes have been developed to synthesize nanoobjects with discharges in liquids where electrodes are submerged. However, these processes can be broadly classified into two main categories: "solution plasma" and "glow-discharge electrolysis", even though some authors use these terms interchangeably. The distinction between these processes is based on two ranges of applied voltages: below or above ~1 kV, which also corresponds to two ranges of interelectrode gap distances: below or above ~1 cm. This dichotomy arises from the use of two types of widely-spread DC power supplies that provide high pulsed voltages or low continuous voltages.

In the case of high-pulsed voltage supplies, no electrolysis precedes the discharge, which ignites by breakdown of the liquid dielectric (most often aided by the presence of bubbles). The transition from electrolysis to glow-discharge electrolysis is characterized by the occurrence of pulsed discharges through a dielectric gaseous sheath as well as current pulses. Plasma electrolytic oxidation is a form of glow-discharge electrolysis, but the applied voltage is usually high enough (several hundreds of volts) to cause the breakdown of the growing oxide layer. While this process can be used for particle synthesis, it is more challenging to control, as its primary purpose is to convert metallic surfaces into oxides [23].

The most commonly used process for synthesizing nanoobjects is known as "solution plasma", although it goes by various other names. This process involves creating a discharge between metallic electrodes submerged in an electrolyte, which may be loaded with chemicals. Electrode erosion and electrolyte reduction can be used separately or together to create nanoobjects and hierarchical structures.

The discharge can also be used to create defects and activate the surface of pre-existing nanoobjects in the liquid. The process was first proposed by Takai [24] and Saito [25] and it is characterized by the following features (see **Supplementary Material 1. Table S1**): Two wire electrodes facing each other, partly covered by insulating materials, are subjected to a unipolar or bipolar pulsed DC high voltage (typically 1 kV) while submerged in a conductive electrolyte. Frequencies are generally in the kHz range, and pulse widths are typically around one microsecond. If the electrodes are hollow or pipes are placed around them, gas (such as N_2 or Ar) can be blown through, which connects them with a bubble. The solution is typically stirred at several hundred rounds per minute and may be controlled for pH, electrical conductivity, and temperature (see **Fig. 2a**). The characteristics of the nanoparticles produced by this process strongly depend on the applied current densities.

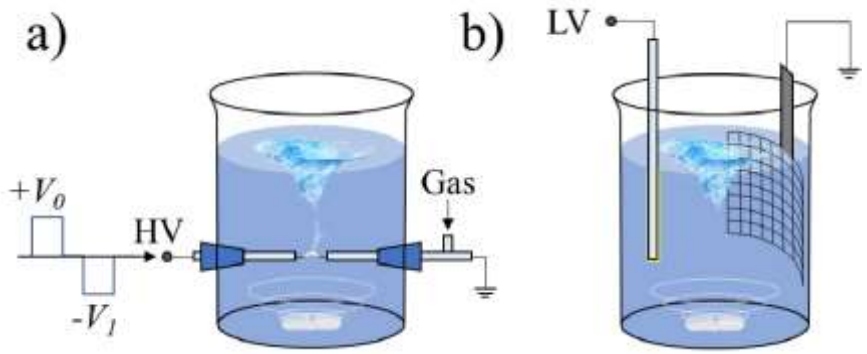

Fig. 2 a) Schematic of the “solution plasma” process. b) Schematic of the “Glow-discharge electrolysis” process.

NP*	V*	I*	w*	f*	Electrodes	Gap	Electrolyte	Vol.*	t*	T*	SS*	pH / *s**	SD*	Gas	Comment	Ref.
	[kV]	[A]	[µs]	[kHz]	[mm]	[mm]		[mL]	[min]	[°C]	[rpm]	[-] / [µS/cm]	[nm]	[sccm]		
MnO_2 ER	*±0.6 -1*	*0-5*	2	15	W		1g $KMnO_4$, 0.15g glucose in H_2O	100	10		Yes		20-100			[9]
Ndop. nanoC ER	*±1.5*	13	0.5	30	W(0.8)	1	Pyridine	200	30		Yes		Sheet:1µm Sphere: 10		w/ or wo/ low-pass filter sheet/sphere	[20]
Au EE*	±1		0.5	20	A/K: Au	0.2	0.5-5 mM NaCl	35	10		450	~6.5/[91-630]	7.6 ± 2.6 @ 0.5mM		ageing increases size	[26]
$BiVO_4$ ER*	±2				W/hollow-W		0.4g $BiVO_4$ in KCl	150	480	Reg.		Adj. w/ NH_3 to 1.5/0.3	6 ± 3	N_2	Chem. synth. of $BiVO_4$	[27]
SiOC	DC: 6-13	< 50				3	HMDSO	40	0.5					Ar/He (300)	600 V in AC current	[28]
B/Fdop.-C ER	±1.5		0.5	100	W(1)		10 mM TPBO, TFPB, TDFPB, TTFPB in toluene	100	20		Yes		20-40			[29]
C ER	±1.5		0.5	50-125	W(1)		Tributylborate	80	60				Flake / NP		Trace W in C	[30]
AuPt EE	>± 0.86	0.6	1-2	10-20	Au(1)/ Pt(1)	0.3	H_2O or ethanol			~0	Yes	[-]/200	1.5 ± 1		Alloying = f(gap)	[31]
C-dots ER	2			20	W(3)	1-2	H_2O/ethanol (1:1)	100	240	10			~3	N_2	On HNb_3O_8 nanosheets	[32]
C ER	±0.6 -1	0-5	0.5-2	100/ 150	W(1)	0.75	Benzene(50mg/L) BZ-NO_2(18) BZ-NH_2(50)		30		Yes		15–25		R: 50 mg/min BET: 220 m^2/g	[33]
WC@C EE-ER	*±0.6 -1*	*0-5*	2	100-180	W(1)	0.5-1	Palm oil	200	30		Yes		4-12			[34]
Poly-pyrrole ER	±6.1	±0.03	100	5	W(0.5)/ (Teflon/Cu (plate))	2	Pyrrole	15	120	40		[8-9]/[0.3-1.5]	2000-20000	Ar(100)	Biased (+ and -) bipolar pulse	[35]
Black-TiO_2 EE	*±0.6 -1*	*0-5*	2	20	Ti(1)		KCl (0.3-3mM) HNO_3 (0.3-3mM)	200	60-240			~6/[66-371] ~1.5/[244-1015]	400-3200		R:13-46 mg/h	[36]
PANI ER	±16.4		60	5	W	1	Aniline	26	20 or 50				~50-200	Ar(100 or 500)		[37]
Ndop.C-dots	±2	1	1	50	W(1)	0.5	Pyridine: H_2O(7:3)	100	10		Yes		6.1 ± 0.7			[38]
Pdop.C-balls	±2		1	100	WC		Liq. $P(C_6H_5)_3$		10		Yes					[39]

ZnO Nbullets. EE	*±0.6 -1*	*0-5*	1	100	Zn(2)-wire Zn(1)-coil	6	H_2O	500	60		200	<100		[40]
ZnO struct. EE-ER	*±0.6 -1*	*0-5*	1	100	Zn or W		$Zn(NO_3)_2$:$6H_2O$ (25 mM), $C_6H_{12}N_4$ (25 mM)	200					Zn = Nrods W = Nplates	[41]
C NPs ER	±1 or 2	0.3-3	100	5	W(1.2)	1	10g sucrose in H_2O	15	0-30		1000	50-200	w/ or wo/ ballast resistor (1kΩ)	[42]
B/Ndop. nanoC ER	±2		0.5	100	W(0.8)	1	200 mM $B(OH)_3$ in Pyridine		5			50-120		[43]
Fe_3O_4 ER	0.25		5	30	W	1	$FeCl_2$:$4H_2O$ +CTAB			25	Yes	40-100	Extern. Cool @ -5°C	[44]
Sdop. nanoC ER	±2		0.5	100	W(1)		BZ+thionanizole	200	20			10-20		[45]
Pt EE	*±0.6 -1*	*0-5*	1-2	15-20	Pt(1)	0.3	Ethanol					2-5	Deposited on CoO_x@N-C	[46]
Pt EE	*±0.6 -1*	*0-5*	0.8	20	Pt	0.5	Ethanol: H_2O (50:50)	80	5-20		500	2-5	Deposited on Ketjen Black	[47]
H_2-Gas ER	±4 (AC)	~4	0.8	30	W(1)	0.7-1.8	Saccharides and alcohols		5-30	5 or 25	No		Power set by gap distance	[48]
NanoC ER	±1.7		1	15	W(1)	0.5	hexane, hexadecane, cyclohexane, BZ						R: 0.16-10 mg/min	[49]
CeO_2 ER	0.8		2	30	W	1	2mM $Ce(NO_3)_2$	300	0-25		Yes	1-10	Mean size lowers with time	[50]
Oligoalginates ER	0.8		2	35			0.1, 0.3, or 0.5% alginate in H_2O		0-60				Reduction of Alginate	[51]
Sn(O_2) EE	-10	[-3-+0.8]	15	40	Sn(1)	0.55-1	H_2O or 10 mg/L gelatine					5 in H_2O 40-400 gel.	R=0.5 mg/min	[52]
Alginate/ Ag-ER	0.8			30	W	1	1−5mM $AgNO_3$ 0.1−0.3% alginate	300	7		Yes	5-40		[53]
Au ER	±1.6		2	15	W(1)	0.3	0.86 mM $HAuCl_4$	150	0-45		400	30-50		[54]
V_xO_y	±1.5		2s	15	W(1)	0.3	0.25 M $VOSO_4$:xH_2O		0-30			Sheets	T evolves freely	[55]

Ag/ Ndop.C EE-ER	*±0.6 -1*	*0-5*	0.8	20	Ag(1)	0.8	2-cyanopyridine	100	30	25	Yes		Ag:10-15			[56]
NanoC	±1.0	[-0.7- +0.7]		5	W(1.2)	1	Alphatic alcohol or hexane		0-40		1000		>80-100		1 kΩ external resistor	[57]
Cu/ Ndop.C EE-ER	±1.0		1	100-200	Cu(4)	0.5	C_3H_7NO	100	60	25			Cu:5-17		Graphene: 1-3 layers	[58]
PtM/ Ndop.C EE-ER	*±1.0*		1	30	Pt+M:Au, Ag, Pd, Pt	1	C_3H_7NO	100	60		Yes		2-8 nm		Bimetallic NP + Graphene: 2-4 layers	[59]
MnO_2/ GO ER	*±0.6 -1*	*0-5*	0.9	25	W	0.5	$KMnO_4$ in 70 mL H_2O+GO in 30 mL H_2O	100	0-20	25	500		MnO_2: 50-80		GO: 0.2-1.8 µm	[60]
TiO_2	2.0		1	20	Hollow W (3ext-1int)	0.3	TiO_2 anatase powder in H_2O		180-900	25				N_2(200)	Brookite is formed	[61]
C and dop.C ER	±1.5		1	20	W(1)	1	BZ	100	30	25	Yes		C, Odop.C, Ndop.C, NOdop.C			[62]
Cu EE	±1.6		3	15-30	Th-W/Cu		Methylene blue 125 mg/L		0-60		Yes		5-10			[63]
C acids ER	±1		0.6	35	W	1-2	BZ+H_2SO_4(0-15%)	100	30		Yes		20-50			[64]
C soots ER	±5		1	80	W(1.5)	1	o-dichloroBZ	80	9	< 38	Yes			Ar: (1 min)		[65]
Fedop. ZnO ER	±2.6 (AC)	2.5-3		0.06	Th-W(2)/ Pt(2)	large	104.2 mg/L $ZnCl_2$ 250 mg/L KCl 5-15 mg/L $FeCl_2$	250	39			8/[-]	28-30			[66]
Polydiacetylene ER	±2		3	30	W	1	Diacetylene, 10,12-pentacosa-diynoic acid	100	0-30	25	Yes		60-100		w/ or wo/ ZnO NPs	[67]
PANI ER	±2.5	[-30-30] µA	60	15	W(0.5)	1	Aniline	26	50			[-] / > 1.3	25-35	Ar(100)		[68]
NanoC ER	±2	[-0.4-0.8] mA	5	20	W(0.5)	1	1-hexanol		20	25-140	1000		10-20	Ar+O_2 (200)		[69]
PANI	±4.0	±4.0 mA	~50	5	W(0.5) / Cu (5)	2	Aniline	23	120					Ar(100)	DBD / bubble block plate	[70]
WO_3 EE	5	0.2-0.5	4	~2 Hz	W(1)	1.5	H_2O	250	10			7	50-170		5 kΩ ballast resistor	[71]

NH_2-C ER	±2		1	15	W(1)	1	0-5 mL APTES, 100 mL ethanol-15g phenol-H_2O 15 g phenol.	100	20		Yes		~10-20		contains silicon BET: 450 m^2/g	[72]
C-dots ER	*±0.6 -1*	*0-5*	0.9	20	W(1)		20mM saccharide in H_2O	100	20		Yes	2, 5, 8/[-]	variable			[73]
GO	2.45	22.4 mA			C(5)/Pt	0.2	0.5 mM KOH 0.2mM$(NH_4)_2SO_4$	500					Sheet:3nm x1.5µm		Exfoliation BET: 130 m^2/g	[74]
Se ER	0-10		0-10	0.1-30	W(3)	30	3mM H_2SeO_3 in H_2O		120		250		100-200		No accurate electrical data	[75]
Au (or Pd, Rh) ER	±2.5		2	20	Hollow-W/W		51 µL 1% $HAuCl_4$ in H_2O+NaOH	100	2	5			Single atom	N_2 (1000)	Au_1 on CeO_2 sheets	[76]
Pt_1@C	20-30	80			C	1	$PtCl_6$						Single atom		Pt_1 in C onions	[77]
Cu-Ni/ CuO-NiO EE	*±1.5*		1-2	15-20	Cu(1)/ Ni(1)	0.3	H_2O				Yes		Mixture of 4 phases			[78, 79]
Au/CuO EE	±1.5		2	20	Au/Cu	0.3	H_2O		45				20-40		R=25 mg/h	[80]
Ag ER	±2.7	2		20	Ag(1)	0.3	28% 0.1mL NH_3 in H_2O	180	20		Yes		12±10 after 75 s		Ag on Ga_2O_3	[81]
N-dop.C ER	±2.8		1	26	W(1)	1	8 mL BZ 40 mL Cyclohexane	48	5		Yes				w/ or wo/ catalysts: Pd, Fe, Cu	[82]
Zn/ZnO		20-150			Zn(3)		H_2O		3		Yes	6.5-7.5 / 0.8-0.9	29-63			[83]

**NP: Nanoparticle. V: Voltage, I: Current, w: pulse width, f: frequency, Vol.: volume, t: treatment time, T: temperature, SS: Stirring speed, σ: electrical conductivity, SD: size distribution. EE: Electrode erosion. ER: Electrolyte reduction. In italic : assumed values.*

Table 1: Selected experimental conditions used with the "solution plasma" process for nanoobjects production.

The other approach, known as “glow-discharge electrolysis”, involves applying voltages beyond those required for electrochemical processes, *i.e.,* a few tens of volts (see **Supplementary Material 2. Table S2**). The electrodes are positioned a few centimeters apart (see **Fig. 2b**) and liquid conductivity must be high enough to transmit charges. As the voltage increases, the current in the solution increases almost linearly, and a gaseous envelope forms around the electrodes due to evolution reactions. When this insulating envelope becomes continuous, the flow of the current stops because shortcuts of conductive liquids fall below the percolation threshold in the sheath. Then, breakdown occurs and discharges appear. At the transition, the current drops and then increases again, but more slowly than before, as the applied voltage increases [84].

Main strategies

There are two primary approaches to synthesizing nanoparticles with solution plasmas and glow-discharge electrolysis. In one approach, electrodes are eroded, emitting vapors that subsequently condense. In the other approach, precursors added to or present in the electrolyte are reduced by discharge electrons at the gas-liquid interface. Both strategies can be used alone or in combination, either simultaneously or successively.

Electrode erosion requires conductive electrodes, with most studies using carbon, metals, or metallic alloys [85]. In this case, electrolyte species are also reduced, which affects the liquid composition and the post-processing of nanoparticles.

Precursor reduction requires refractory metals as electrodes to limit their fusion by discharges and emission of metal contaminants. Tungsten is commonly chosen as it is the most refractory metal, readily available, and has a melting temperature of 3,695 K. Precursors often include metallic salts (chlorides, nitrates, acetates, etc.), carbonaceous compounds (aromatic cycles, alkanes, alcohols, etc.), monomers (HMDSO, APTES, diacetylene, etc.), and bio-sourced materials such as saccharides.

In every situation, three essential sets of parameters must be properly defined to obtain the desired properties of the nanoobjects (**Fig. 3**): solution characteristics, process conditions, and time. Parameters are often strongly interrelated: for instance, the solution’s composition determines its conductivity, which requires a specific voltage signal, leading to current densities determined by the electrode sizes. In the following descriptions of the influence of each parameter, emphasis will be put on the most striking features associated with a given parameter, and coupling with others will be made as clear as possible.

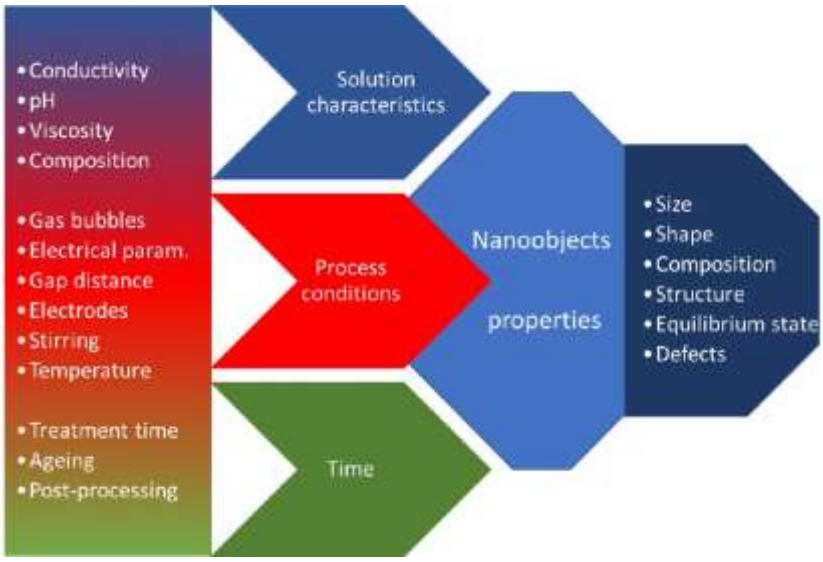

Fig. 3 Links between process parameters and nanoobjects properties

NP*	V*	I*	Gap	Cathode	Anode	Electrolyte	Vol.*	t*	T*	SS*	pH / σ*	SD*	Comment	Ref.
	[V]	[A]	[mm]	[mm]			[mL]	[min]	[°C]	[rpm]	[-] / [µS/cm]	[nm]		
Al	30	~5		Al [5]	Pt	H_2O+(K_2CO_3 / 0.1-0.5 M)	300	30				[140-155]	5 V/min till BD and 30 V	[21]
Al_2O_3-ZrO_2		10(100 Hz)	90	Ti [200^2x1]	Ti	H_2O+(KOH 1 g/L)l	4 L	30	Cooled	Yes		0.1-10 µm	PEO. (T<60°C)	[23]
CuO-ZnO	52-72	~4.6		Brass [0.5]	Pt	NaCl / 2M			Bath	200		[6] Nano-flowers	Brass: 63%Cu-37%Zn	[84]
Cu	110	<4	Large	Cu [1]	Pt	H_2O+(K_2CO_3 or NaOH / 0.1-1M)	300	15				[7-28] µm [38-28] µm	From 0 to 110 V @ 5 V/min	[86]
Fe-Based	0-300	0-2.5		Steel [2]	Steel [Large]	H_2O+(KOH 0.125-0.625 wt%)	400	60	~80	Yes		[0.1-50] µm		[87]
Ti/Au/Zn /C	95-125			Ti/Au/Zn [0.5] C [1]	Ag [1]	H_2O+(K_2CO_3 / 0.1 M)	200					Element-dependent	Preheating @ 5V 60 min	[88]
Au foam	110-150		30	W [1]	Pt grid	H_2O+($HauCl_4$ / 0.03-0.1 M)+acid		10 s		1200			Acid=HCl, H_2SO_4 or HNO_3(10M)	[89]
Na_2FeO_4	20-55	7.3	30	Steel [large]	C-steel [2mm]	H_2O+(NaOH / 8-18M)	500	5	5-45	350	[] / [390-650] mS/cm	[10-90]	Breakdown after delay	[90]
Mn_3O_4	550-650	0.1-0.14		Pt [needle]	Mn [Large]	H_2O+($NaNO_3$ / 2 g/L)	150	60	25	120	[6.5-10.5] / [-]	[14-26] [120-220]	Nanospheres	[91]
Fe_3O_4	600	0.15	10	Pt [large]	Scrap Fe	H_2O+(Na_2SO_4 / 2 g/L)	150	0-60		90	[6-11] / [-]	[0-26]	2 kΩ ballast resistor	[92]
$Ni(OH)_2$	500	0.085	~5	Pt [needle]	Ni [Large]	H_2O+(NaCl / 2 g/L)+ CH_3COONa	150	60	25	120	[6.5-10.8] / [-]	[1-3] µm	2 kΩ ballast resistor	[93]
Mn_3O_4	130	~1		Cu [0.9]	C-Cloth	0.01M $C_4H_6MnO_4$ / 0.5M NaCl	50	10		150		NP: 40nm Nanosheet	H_2O + 9 mg CTAB + 30 mg PVP	[94]

**NP: Nanoparticle. V: Voltage, I: Current, Vol.: volume, t: treatment time, T: temperature, SS: Stirring speed, σ: electrical conductivity, SD: size distribution.*

Table 2: Selected experimental conditions used with the "glow discharge electrolysis" process for nanoobjects production. Electrode erosion only except for Xiu's works [94] based of electrolyte reduction.

Solution characteristics

Electrical conductivity

Electrical conductivity is generally the key factor that determines the applied voltage required for breakdown and discharge ignition. The lower the conductivity, the higher the voltage needed to achieve reproducible discharges, and the shorter the pulse width.

In the experimental results presented in this work, the electrical conductivity ranged from 0.2 to 1015 µS cm^{-1}, which is higher than that of Milli-Q water (~0.06 µS cm^{-1}) but includes deionized water (~10 µS cm^{-1}). Achieving breakdown in these media requires high voltages (> a few hundreds of V) and short gaps (< 1 mm) with currents around several amps. To ensure reproducible breakdown conditions, electrolytes such as NaCl are often introduced. This helps to stabilize the discharge during synthesis [26].

Analyzing the influence of conductivity is not straightforward, as it affects not only all electrical parameters, but also the temperature of the solution. The important concept to keep in mind is that it affects the way the generator supplies the circuit, and this relationship is not linear and varies over time. All generators used in the processes studied here are voltage-driven, with the voltage set at a given intensity, for example with a rectangular shape defined by its width and frequency of occurrence. However, the voltage applied to the power electrode is quite different because of the non-linear answer of the discharge. The behavior of the current is also dependent on the specific generator used.

As the electrical conductivity decreases, a higher breakdown voltage is required to ignite the discharge. Saito *et al*. [95] have stated that "when the concentration of the electrolysis solution [*and thus the electrical conductivity*] is low, the current decreases, and the plasma generation requires a high voltage owing to an increase in the solution resistance." Similarly, Saebnoori *et al*. [96] have observed that solutions with lower concentrations of potassium carbonate exhibit lower current density and higher breakdown voltage due to the lower conductivity of the electrolyte. Anbouri *et al*. [86] have also shown that the same is true for glow-discharge electrolysis. For insulating liquids such as Milli-Q water, heptane, or liquid nitrogen, Belmonte *et al*. [97] demonstrated, using a nanosecond-pulsed electrical switch, that discharges ignite at breakdown voltages beyond a few kV in micro-gaps and generate currents around hundreds of amps without a ballast resistor.

Kim *et al*. [98] assisted the discharge process with oxygen bubbling under the electrodes in water containing concentrations of LiCl ranging from 0 to 15mM. They showed that decreasing the electrical conductivity (from 500 to 2 µS cm^{-1}) was advantageous for the decomposition of methylene blue, although discharge ignition was more difficult. With a similar configuration, Hamdan *et al.* [99] showed that the discharge probability, volume, and lifetime reduce, when the electrical conductivity increases.

In contrast, Shin *et al*. [68], observed a different behavior when assisting the discharge process with argon bubbling around the electrodes. They measured an increase in the breakdown voltage and a decrease in current as the conductivity increased from 0.2 to 1.3 µS cm^{-1}. It is important to note that this decrease in the discharge current occurs over time as the liquid changes, attributed to an increase in the resistance of the discharge. The way in which bubble injection is done with respect to the electrode is therefore crucial. In this example, by-products from decomposition reactions within the liquid gradually modified the composition of the argon gas, which increased the breakdown voltage.

On the other hand, as observed, for instance, by Lee *et al.* [100], too high electrical conductivity (*i.e.*, above 6000 µS cm^{-1} [101]) prevents the occurrence of the discharge.

The same authors [100] note that "too low" electrical conductivity leads to minimal nanoparticle production. This is because the conductivity is determined by the concentration of the precursor, so if it is low, the conductivity and production yield will be low as well.

This behavior can also be caused by an increase in circuit resistance, which decreases the current provided by the power supply at a given voltage. If the current is not limited by the generator, as demonstrated in [102], significant nanoparticle production (~0.1 g h^{-1}) can still occur in liquids with electrical conductivities as low as 0.06 µS cm^{-1}. In electrode erosion-based processes, nanoparticle production is dependent on the charge delivered to the electrodes, as demonstrated by Hamdan *et al*. [103], which is controlled by the internal capacitance of the generator.

According to Lee *et al*. [100], there is little difference in the morphology of tin nanoparticles produced from $SnCl_2$ when the electrical conductivity changes, whereas their size slowly increases with an increase in electrical conductivity. The same group showed that an increase in the initial conductivity, as well as the conductivity during treatment, leads to bigger Ni nanoparticles [104].

In glow-discharge electrolysis, Anbouri *et al*. [86] showed that size evolution can vary depending on the electrolyte. With a higher concentration of K_2CO_3, and thus higher conductivity, the size of copper nanoparticles increases, but it decreases in NaOH. This behavior is attributed to a lower amount of nanoparticles being produced in NaOH as the concentration increases. This means that NaOH modifies the characteristics of the discharge in such a way that electrode erosion is less efficient. However, no mechanism is given to explain how this happens.

pH

In general, the pH of a solution influences the reaction pathways in acidic or basic environments. When precursors are dissociated, the pH determines which intermediate products react preferentially with H or OH. It also plays a crucial role in defining the electrical stability of the synthesized phases.

The impact of the pH is particularly significant, as demonstrated by the Pourbaix (potential–pH) diagram (**Fig. 4**), which shows how the electrochemical stability of the synthesized phase varies with this parameter. For instance, Saito *et al*. [105] synthesized Cu/CuO nanoparticles via glow-discharge electrolysis. In a basic solution, made of K_2CO_3 with concentrations ranging from 0.001 to 0.50 M, CuO nanoflowers were formed. In an acid solution buffered by citrate (pH=4.8), spherical particles, possibly with pores, were formed. When the eutectic phase Cu/Cu_2O was present, Cu_2O was dissolved as predicted by the Pourbaix diagram, leading to the formation of pores. During the electrolysis, the copper cathode was negatively charged, which stabilized metallic copper. When the cathode surface melted and generated nanoparticles, the particles that peeled off from the surface had zero potential. Conversely, the potential in the sheath could reach tens of volts, making equilibrium conditions irrelevant for this type of analysis.

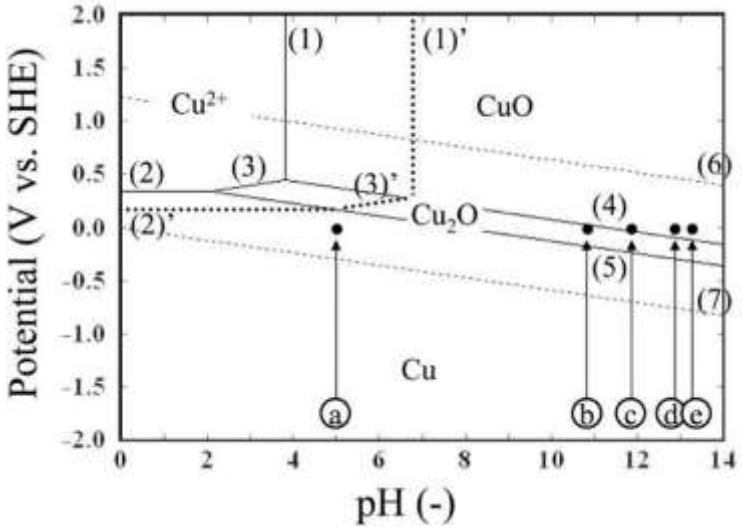

Fig. 4 Pourbaix diagram of copper. (Color online) Cu E–pH diagram under the assumption of $[Cu^{2+}] = 1.0$ mol/kg (solid line) and $[Cu^{2+}] = 1.0\times10^{-6}$ mol/kg (dotted line); (1) $CuO + 2H^+ = Cu^{2+} + H_2O$; (2) $Cu^{2+} + 2e^- = Cu$; (3) $Cu_2O + 2H^+ = 2Cu^{2+} + 2e^- + H_2O$; (4) $2CuO + 2H^+ + 2e^- = Cu_2O + H_2O$; (5) $Cu_2O + 2H^+ + 2e^- = 2Cu + H_2O$; (6) $2H_2O = O_2 + 4H^+ + 4e^-$; and (7) $2H^+ + 2e^- = H_2$. The plots show the pH of solutions which were used in the experiments; (a) citrate buffer (pH=4.8), (b) 0.001 M K_2CO_3; (c) 0.01 M K_2CO_3; (d) 0.01 M K_2CO_3; and (e) 0.5 M K_2CO_3. SHE means standard hydrogen electrode. After Saito *et al*. (2011) J Appl Phys 110:023302. Reproduced with permission from the American Institute of Physics.

Bratescu *et al*. [106] demonstrated that the reduction of $HAuCl_4$ by solution plasma in the presence of CTAC (hexadecyltrimethylammonium chloride) produces nanoparticles with diameters smoothly decreasing from 10 to 2 nm as the pH of the solution increases from 3 to 12 by adding small amounts of 1M NaOH. The conductivity of the solution measured before and after experiments did not vary monotonically with NaOH concentration, confirming the main role of pH variation on the observed changes in nanoparticle size. Surface functional groups differ with pH, with CTAC-originating ligand-metal complexes forming at pH 3 and oxygen binding with metal at pH 12. The pH modification alters the initial ion state of the precursor and the redox standard potential of the reactions it undergoes. Electrostatic repulsion forces between gold ions and the protective layer of the surfactant also contribute to explaining the observed experimental results.

By adjusting the pH of solutions containing saccharide precursors (with a pH around 5 without additives) between 2 and 8 with HCl and NaOH, Treepet *et al*. [73] showed that carbon dots produced by solution plasma only emit light for pH values greater than 5. The pH value directs chemical reactions towards intermediate by-products resulting from precursor decomposition by the discharge. It plays a crucial role in chemical pathways and can be used to some extent to drive polymerization processes.

Mn_3O_4 microspheres, made of two types of nanospheres (small and large, with the latter resulting from the aggregation of the former), were produced by Wang *et al*. [91] using glow-discharge electrolysis. During the production process, the pH of the solution gradually increased from around 6.5 to approximately 10.5 within 30 minutes, after which it stabilized. However, the pH varied spatially, depending on the proximity to the anode (acid, pH < 3) or the cathode vicinity (basic, pH > 10). Mn^{2+} ions were produced at the anode and then transported to the cathode, where they reacted to form $Mn(OH)_2$. In basic conditions, $Mn(OH)_2$ was oxidized to form MnOOH, which then reacted with manganese oxides to produce Mn_3O_4.

In a similar process, the same group synthesized Fe_3O_4 nanoparticles and observed an increase in pH from 6 to 11.5 during the treatment of a solution containing 2 g L^{-1} of Na_2SO_4 [92] (see also [93] for $Ni(OH)_2$ nanoflowers). Fe_3O_4 nanoparticles were found to be stable in highly alkaline aqueous media. The formation

mechanism is similar to that of Mn_3O_4, with the spinel form of iron oxide resulting from the reaction of Fe^{2+} and Fe^{3+} ions in the presence of OH^-. Fe^{3+} ions were produced at the cathode by oxidation of Fe^{2+} ions.

Viscosity

In general, viscosity plays a critical role in particle transport and prevents their agglomeration.

Vanecht *et al*. [107] reported evidence that the growth of Au nanoparticles sputtered by physical vapor deposition in ionic liquids was faster in less viscous media. For comparison, it is important to note that viscosity was varied from 0.032 to 0.354 Pa s.

Treatments of alginate solution [51] showed that the initial viscosity of solutions with various alginate concentrations (ranging from 0.1 to 0.5% w/v) decreased strongly, from 0.0246 Pa s (for the most concentrated) to 0.0024 Pa s in 15 min of discharge, and to 0.0018 Pa s in 30 min, with no further changes observed thereafter. Fragmentation by the discharge shortened the long-polymer chains, which led to a decrease in viscosity. This behavior generally depends on the concentration and molecular weight of the precursor through the Kuhn–Mark–Houwink equation [108]. Similar behaviors were observed with other natural polymer-based materials [109] like cellulose [110, 111] or chitosan [112-114].

Contrary to cellulose and chitosan, the viscosity of gelatin-containing solutions can either decrease due to depolymerization (at 40 °C) or increase due to cross-linking (at 22 °C) [115, 116]. At low temperature, the formation of free radicals in the solution triggers enhanced cross-linking in gels, leading to an increase in solution viscosity. As expected, depolymerization of gelatin at higher temperature results in a decrease in solution viscosity.

Cross-linking has also been observed with solutions of monomers such as aniline [68], where the viscosity increases as PANI is produced. The synthesis of free radicals was likely favored over the dissociation of aniline by applying ultra-mild discharge conditions, *i.e.*, with currents below 30 µA in absolute value.

Composition

The composition of a solution typically consists of several components, including:

- *the carrier liquid, which is most often water but can also be non-aqueous liquids such as liquid nitrogen or alcohols,*
- *the selected electrolytes (such as NaCl, KOH, $NaNO_3$, etc.) and surfactants (anionic surfactants like sodium dodecyl sulfate-SDS or cationic surfactants like cetyltrimethyl ammonium bromide-CTAB),*
- *the precursors (such as $HAuCl_4$, $CuCl_2$, $FeCl_2$ or $FeCl_3$, etc.), which can have different structures (such as benzene, alkanes, alkenes, etc.)*
- *the presence of dopants (such as triphenylphosphine, boric acid, thioanisole, etc.)*

Non-aqueous solutions

Among the most often used non-aqueous liquids, carbonaceous compounds and liquid nitrogen occupy a special place. The structure of carbonaceous compounds plays a key role in the formation of nanoobjects, and will be discussed in more detail in the corresponding paragraph.

Liquid nitrogen is preferred over water or alcohols to suppress oxidation processes during the synthesis process. It can also be used to produce nitrides [117] or to dope materials with nitrogen [118]. The reason why Park *et al*. were able to synthesize nitride nanoparticles from aluminum, whereas Hamdan *et al*. [119] could only obtain metallic aluminum, is still unclear. However, the maximum current intensity reached at the beginning of the discharge could explain this difference. In Hamdan *et al*.'s work, current reaches up to 150

A, compared to 5 and 30 A in Park *et al*.'s experiments. The formation of a fully metallic discharge at very high current, with negligible incorporation of nitrogen, would thus limit metal nitriding.

Although the temperature of liquid nitrogen is very low, the intense evaporation of the metastable liquid during the discharge prevents proper thermal exchange between the produced substance and its surroundings. Thus, the cooling efficiency of liquid nitrogen is lower than that of deionized water [120]. Therefore, it is difficult to accept, as proposed by Üstün *et al*. [121], that "the sharp temperature gradient from the arc zone to the liquid nitrogen medium plays a vital role in producing different nanoparticles with various morphologies". Furthermore, the temperature difference between the plasma core and the liquid is only 2% larger with liquid nitrogen than with water, as the plasma temperature is around 1 eV (~12000 K).

Electrolytes concentration

Horiguchi *et al.* [122] demonstrated that the frequency of plasma emissions and the size of Pt nanocrystals depend on electrolyte concentration in the presence of intentionally injected microbubbles in the liquid. The frequency of plasma emissions increased as the concentration of KNO_3 increased due to the simultaneous increase in the solution's conductivity. In contrast, Pt nanocrystal size initially decreased as KNO_3 concentration increased, showing a minimum size of 3.3 nm at 2.06 mM KNO_3; but then increased with further electrolyte concentration. At high KNO_3 concentration, the increase in frequency of plasma events caused an increase in Pt concentration in the solution plasma, which favored the production of larger Pt nanocrystals. These results indicate that by varying the conductivity of the solution, the frequency of plasma emissions and the size of Pt nanocrystals can be controlled.

Reprocessing of already-synthesized nanoobjects can be limited by large volumes of vessels, which makes flowing processes, such as overflow or more sophisticated microfluidic systems, a natural choice [122].

Chantaramethakul *et al*. [26] used a solution plasma process and observed that gold nanoparticles, immediately after processing, became smaller as the NaCl concentration increased from 0.5 to 5 mM. They associated this result with weaker erosion yields caused by higher electrical conductivities.

Anbouri *et al*. [86] observed in glow-discharge electrolysis that the size of copper nanoparticles increases as the concentration of K_2CO_3 increases from 0 to 1M. In contrast, it decreases when NaOH concentration, used instead of K_2CO_3, increases also from 0 to 1M. This behavior is attributed to the way the discharge erodes the electrodes, as discharges are weaker (the glow is said to be not "full") in NaOH beyond 0.5M. Yii *et al*. [123] also observed with TiO_2 nanoparticles that their mean size increases when the concentration of K_2CO_3 increases from 0.1 to 1M.

In the case of K_2CO_3 and NaOH at concentrations higher than 0.1M, the pH is higher than 10, and this parameter has little influence. Some observations confirm that increasing the concentration of the electrolyte can have a more complex effect on size distributions than simply increasing the electrical conductivity of the solution and weakening discharges.

Surfactants

In general, the addition of surfactants like sodium dodecyl sulfate (SDS) or cetyltrimethylammonium bromide (CTAB) stabilizes and disperses the synthesized nanoparticles in solution [124].

Lee *et al*. [104] synthesized alloyed nanoparticles made of nickel and copper with traces of tungsten using a solution plasma process. They found that the addition of an anionic surfactant (SDS) had no significant effect on the size of the nanoparticles, while the addition of a cationic surfactant (CTAB) up to 20% resulted in smaller spherical particles. However, beyond 30% of CTAB, the particles became polygonal, large, or whisker-shaped.

Lu *et al*. [125] were able to change the shape of the CuO nanoobjects produced by glow-discharge electrolysis by adding CTAB to the solution (**Fig. 5**). They obtained spindle-like CuO nanoparticles formed by the assembly of smaller nanoparticles (~20 nm) at an applied voltage of 300 V. Increasing the applied voltage to 350 V made the reaction "very violent" and resulted in the formation of larger aggregated particles. Thus, the discharge likely modifies the surfactant by reducing it, affecting its chemical properties and its ability to prevent particle agglomeration.

The same group [126] suggested that adding CTAB only changes the growth pattern of Ta_2O_5 crystallites rather than influencing the composition of Ta_2O_5 nanoparticles using the same process.

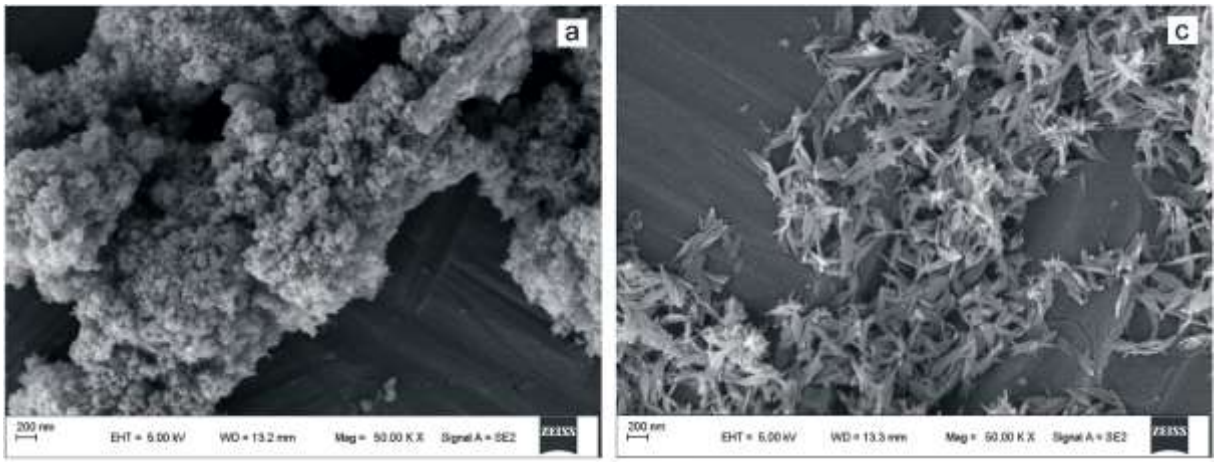

Fig. 5 SEM images of CuO nanoparticles prepared without CTAB (left) and with CTAB (right). After Lu *et al*. (2020) Mater Lett 264:127316. Reproduced with permission from Elsevier.

Musaka *et al*. [52] demonstrated that the average diameter of tin nanoparticles produced by wire erosion was non-linearly dependent on the concentration of gelatin, used as a surfactant in water, with a minimum value at 2 mg/L. Although the observed behavior is not fully understood, it may be attributed to an optimal activation of gelatin by the discharge for a certain production rate of tin. Additionally, the use of surfactant prevents metallic nanoparticles from oxidizing to SnO_2.

Structures of precursors

The structure and concentrations of precursors play a key role in the synthesized products. It is well known, for instance, that the choice of carbon precursor structure strongly determines the forms of nanocarbons produced by plasma. Solution plasmas also obey to these rules.

Morishita *et al*. [49] investigated the synthesis routes of nanocarbons by solution plasma from hexane, hexadecane, cyclohexane, and benzene. Benzene provides the highest production rates, which is not astounding since the carbon-hydrogen homolytic bond dissociation energy for benzene is considerably larger than for cyclohexane and linear molecules. Two main routes are described, depending on the structure of the carbon precursor. Cyclic molecules would produce intermediates like benzene radical cations, which are assumed to polymerize at the discharge-liquid interface. On the contrary, linear molecules are first fragmented and form shorter olefins, starting from C_2, and these fragments assemble in a second step by pyrolysis (heating in the plasma), leading to more crystalline nanocarbons than cyclic molecules. This scheme assumes that dissociation processes in the discharge and at its interface with the liquid are relatively similar for linear chains but different for cyclic molecules, as cyclic molecules must be opened and fragmented within the discharge (1.7 kV is applied with currents around several amps, representing a huge power density in small plasma volumes). As the energy deposited at the edge of the plasma is much weaker than inside, cyclic molecules are likely preserved at the boundary.

Islam *et al*. [33] compared the effects of grafting different functional groups on benzene by comparing C_6H_6 to aniline (NH_2-C_6H_5) and nitrobenzene (NO_2-C_6H_5). As expected, the resulting nanocarbons exhibited different chemical structures, including C-N and N=O bonds for nitrobenzene and C-N and N-H bonds for aniline. In the latter case, the number density of defects sites was higher. However, all nanocarbons were spherical with very similar average diameters (15-25 nm) and BET surface areas (~220-230 m^2/g). They adopted graphite-like structures with a good nanocarbon crystallinity. Benzene provided the highest production rates. Experimental conditions were very close to Morishita's – where initial concentrations are unknown – except for the frequency, which was 10 times higher (150 kHz vs 15 kHz) and production rates, which were 5 times higher (50 *vs* 10 mg min^{-1} for benzene). Thus, the deposited power, with initial concentrations being relatively similar, certainly contributed to higher fragmentation of cycles, leading to nanocarbons with features that were closer to those produced by the pyrolysis route in this case.

Romero Valenzuela *et al*. [65] used o-dichlorobenzene, a benzene ring with two chlorine atoms, to produce carbon soot as a precursor for the growth of fibers. The conditions were chosen to retain chlorine in the soot in order to create defects in nickel used next as a catalyst. Although plasma conditions are similar to Islam's, chlorine was found in the resulting carbon particles. These particles were large (0.39 to 1.7 µm) but made up of coalesced smaller spherical particles.

Park *et al.* [57] used a similar approach to investigate six aliphatic alcohols (from methanol to hexanol) and n-hexane as precursors for synthesizing nanocarbons. The presence of oxygen in the precursor molecule, and consequently the C/O ratio, strongly affects the morphology and the degree of graphitization of the synthesized nanocarbons. The highest C/O ratios (in 1-hexanol – C/O = 6 – and n-hexane) result in the highest degree of graphitization and the lowest content of flakes relative to spheres (no flakes are observed in n-hexane).

Shin *et al*. [69] synthesized nanoparticles in 1-hexanol using a solution plasma assisted by Ar/O_2 bubbles injected in the interelectrode gap. Breakdown occurred in the gas phase around 1-2 kV, with currents remaining below 1 mA, providing "mild" discharge conditions. The level of graphitization was enhanced using Ar:O_2 mixtures (3:1), where the production of oxygen atoms was maximal. It is known that Ar-O_2 mixtures exhibit maximum dissociation of O_2 for amounts of oxygen in argon close to this ratio, leading to higher concentrations of O atoms than in pure O_2 [127] and, of course, pure argon. Therefore, higher O_2 contents in argon result in lower graphitization. Regardless of the gas composition, the particles are always spherical. If this conclusion aligns with Park *et al*.'s findings [57], the role of oxygen here is drastically different, as oxygen in the gas phase must play a specific role. Further investigations are needed to determine the role of bubbles in the way oxygen active species are created.

Huang *et al*. [32] demonstrated that carbon dots (~3 nm in size) can be anchored onto HNb_3O_8 nanosheets introduced in ethanol – C/O = 2 – and processed by solution plasma. The presence of the nanosheets in the liquid certainly affects the growth mechanism of the carbon products. Carbon dots are chemically bonded to HNb_3O_8 nanosheets, which results either from heterogeneous growth or, more likely, from attachment of already-grown clusters to defects created by the discharge in the nanosheet lattice. As carbon dots are ultra-small, it is difficult to say whether these results, based on ethanol where the C/O ratio is low, are in line with Park's findings [57].

Treepet *et al*. [73] selected three relatively simple saccharides (5-membered ring (fructose), 6-membered ring (glucose) and their combination (sucrose)) to synthesize nanocarbons by solution plasma. Usually, saccharides are used to produce hard carbons. The conditions are close to those used by Kum *et al*. [42], but the frequency is four times higher and the pulse width is 0.9 µs instead of 100 µs. Considering the type of precursor, the degree of graphitization changes in the following order: Fru-CDs > Glu-CDs ~ Suc-CDs, showing the orderliness of in-plane sp^2 carbon atoms in the core of Fru-CDs. The size of the carbon dots is proportional to the precursor's molecular weights: Fru-CDs < Glu-CDs < Suc-CDs, but the average size

increases at higher pH. These results are interpreted through comparison with the mechanism steps proposed by Morishita *et al*. [49]: nanocarbon formation starts from (i) C-H dissociation, followed by (ii) conversion into unsaturated ring molecules, and (iii) polymerization through cation radicals. The authors attributed the higher degree of graphitization of the carbon dots produced from fructose to the 1,2-enediol intermediate specifically produced by 5-membered ring molecules (**Fig. 6**). Sucrose would also be less graphitized because of its disaccharide structure.

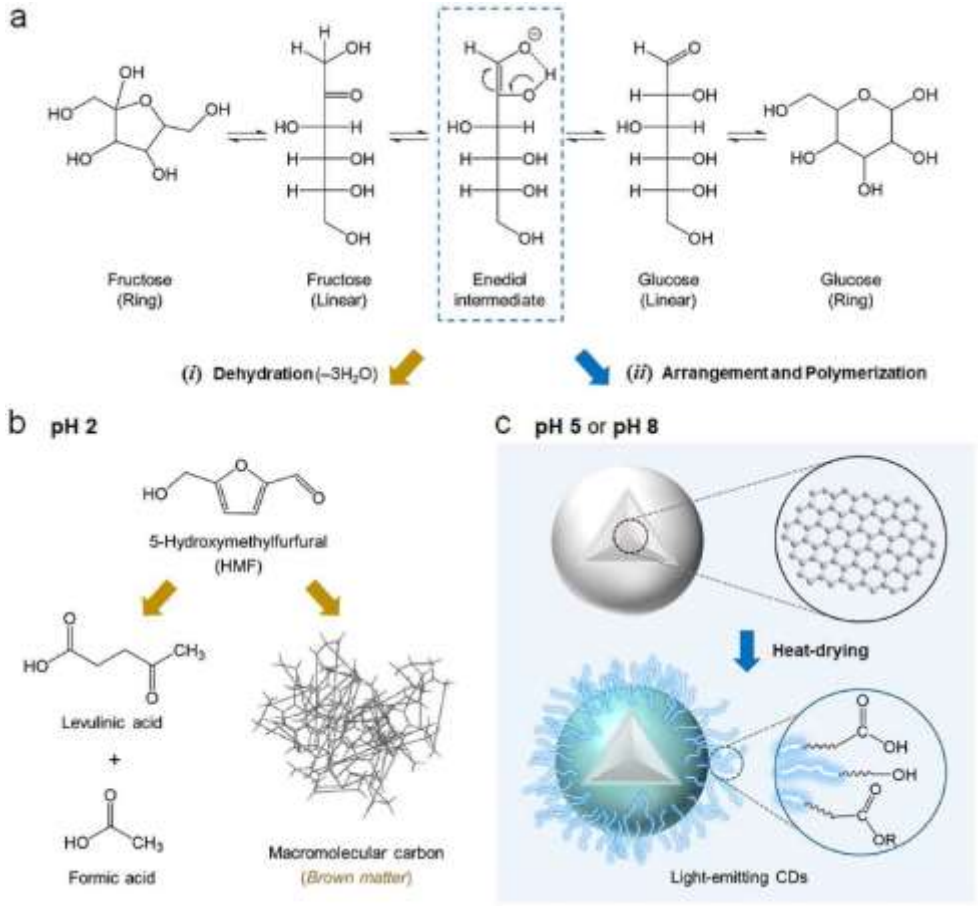

Fig. 6 Schematic illustration of possible reaction pathways for CD formation through SP from fructose and glucose. Starting from (a) isomerization between glucose and fructose occurring under acidic and alkaline conditions through the 1,2-enediol intermediate formation. Possible reaction pathways and the related products in (b) acidic media (pH 2) and (c) pH 5 and 8, along with the post-treatment aid by heat-drying. CD, carbon dot; SP, solution plasma. After Treepet *et al*. (2022) Mater Today Chem 26:101139. Reproduced with permission from Elsevier.

Sucrose ($C_{12}H_{22}O_{11}$, low C/O ratio ~1) was used as carbon source by Kum *et al*. [42]. Carbon nanomaterials synthesized from sucrose have an average size ranging from tens to hundreds of nanometers. They exhibit absorption spectra similar to those of graphene and graphene oxide.

Chokradjaroen *et al.* [30] observed that carbon products synthesized by solution plasma in trimethyl borate are negligible, limited in triethyl borate, and by-products are all decanted. The particles are larger with tributyl borate where a fourth of the mass of nanocarbons remains in suspension. In this case, boron (and traces of tungsten from the electrodes) was detected on nanocarbons in suspension, but no carbon-boron bond could be detected by XPS. The decanted particles are flakes-like structures (with ~45 carbon monolayers), whereas nanocarbons in suspension are made of fullerene-like multilayers surrounded by a disordered amorphous phase.

Ualkhanova *et al*. [128] investigated the synthesis of spherical nickel particles encapsulated in a graphene shell using discharges in water, ethanol, and toluene. They eroded a nickel wire facing a carbon electrode. Nickel particles synthesized in water and alcohol were covered by a multilayered graphene shell, with more defects in water than in ethanol. They also contained a nickel oxide phase, probably as a shell as well, formed by the oxidation of nickel in the liquid. As toluene does not contain any oxygen, it enables the complete encapsulation of nickel particles by carbon, which prevents surface oxidation of the samples. The large amount of carbon in the composition of toluene promotes the formation of metastable nickel carbide that can be removed by annealing at 300°C in argon.

Doping

Plasma processing in solutions can be used to graft different functional groups onto carbon networks and modify surface interactions. Additionally, atoms can be inserted inside the network by substituting a carbon in a ring, which can enhance the catalytic properties of nanocarbons.

Nitrogen is an important element for this purpose and has been extensively studied. Precursors such as pyridine (C_5H_5N) [20, 38, 43, 82], aniline ($C_6H_5NH_2$) [129], APTES (*i.e.,* $SiO_3(C_2H_5)_3C_3H_6NH_2$ or 3-aminopropyltriethoxysilane) [72] or DMF (*i.e.,* C_3H_7NO or *N*,*N*-dimethylformamide) [58, 59] can be used to introduce nitrogen atoms (see **Fig. 7a**). Bratescu *et al*. [129] demonstrated that discharges in aniline result in much lower concentrations of CN radicals compared with discharges in pyridine.

N atoms in carbon rings can be pyridinic, pyrrolic, or graphitic (or quaternary N). Due to their five-valence electrons, they can cause the planar carbon structure to bend. However, plasma processes can introduce a cationic type of N-dopant with four-valence electrons, which preserves the planar structure of carbon [130] (**Fig. 7b**).

High-resolution XPS is a useful technique to determine the different types of bonds present in amino-modified nanocarbons (**Fig. 7c-e**). The N-1s spectrum is typically deconvoluted into four components, namely pyridinic-N at 399.0 ± 0.5 eV, pyrrolic-N at 400.0 ± 0.5 eV, cationic-N/graphitic-N at 401.0 ± 0.5 eV, and pyridinic-N oxide (NO) at 402.5 eV. The high-resolution peak in the C-1s region can be interpreted by considering the presence of different types of carbon bonding: C=C bond (284.5 eV), C–C bond (285.0 eV), C–N bond (285.9eV), C–O bond (286.5 eV), and C=O bond (287.0 eV). Lee *et al*. [20] assert that the presence of the C–N bond at 285.9eV proves the successful incorporation of nitrogen into the carbon structure. However, it only proves the presence of C–N bonds that can possibly be perpendicular to the ring basal plane. Kim *et al*. [38] took more precautions by interpreting the high-resolution XPS spectrum of C-1s with only a two-peak deconvolution at 284.6 and 286.1 eV, corresponding to C=C, and C–N/C–O bonds. The contributions of C–N and C–O are relatively close, and the unexpected presence of oxygen makes spectra analyses more complicated. These authors also provided the high-resolution XPS spectrum of O-1s with two peaks: one peak at 531.2 eV attributed to C=O, and one peak at 532.6 eV attributed to C–O.

The presence of nitrogen atoms in the carbon networks of nitrogen-doped graphitic carbon nanosheets produced by Lee *et al*. [20] is demonstrated by the catalytic activity of the nanoparticles, which enhances the oxygen reduction reaction (ORR) activity. Thanks to amino-functional groups present in N-doped carbon dots (~6 nm in diameter) produced by Kim *et al.* [38], the dots exhibit bright blue fluorescence. This fluorescence can be quenched by 2,4,6-trinitrophenol, which can thus be detected.

It is possible to nitride oxygen-doped nanocarbonaceous sorbents by NH_3-treatment at 800 °C [62]. The raw XPS N-1s spectra provided in this work are noisy and binding energies of pyridinic-N (given at 384 ± 0.1 eV) and pyridinic N-oxide (at 403.5 ± 0.2 eV) are pretty far from the values given above. However, these sorbents exhibit a higher CO_2 adsorption capacity.

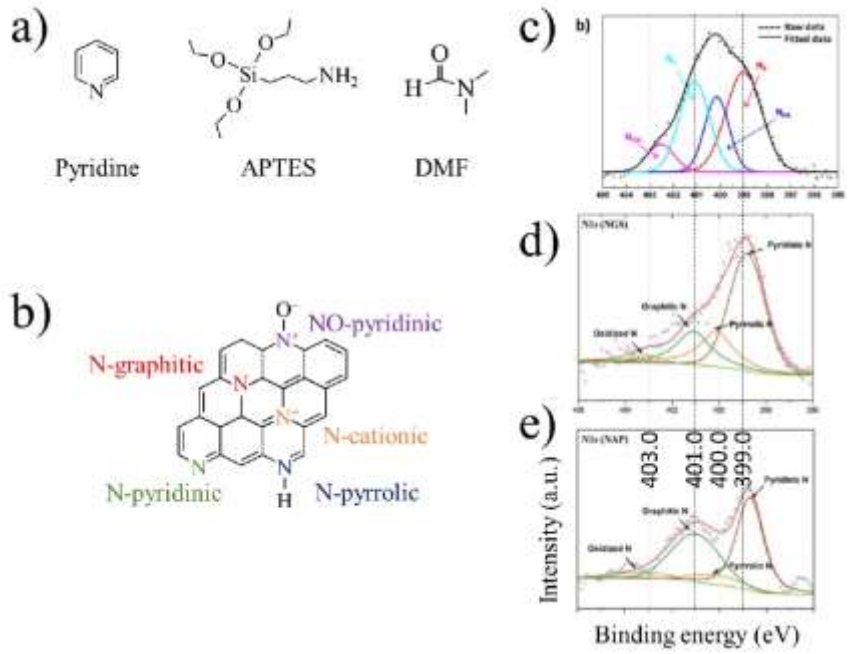

Fig. 7 a) Some precursors used to dope nanocarbons with nitrogen. b) The different possible states of nitrogen within the carbon network. c) High-resolution XPS spectra of N-doped nanocarbons by [38]. After Kim et al. (2020) Carbon 168:448−457. Reproduced with permission from Elsevier. d) idem by [20] for nitrogen-doped graphitic carbon nanosheets (NGS) synthesized with a tune-up SP system including a low-pass filter circuit. e) idem by [20] for nitrogen-doped amorphous carbon nanoparticles (NAP) synthesized with standard SP system. After Lee & Saito (2018) RSC Adv 8:35503−35511. Reproduced with permission from RSC Publishing.

The tune-up solution plasma system, proposed by *Lee et al*. [20] and based on the use of a low-pass filter circuit, provides appropriate plasma conditions for synthesizing nitrogen-doped graphitic carbon nanosheets where nitrogen atoms do integrate, at least to some extent, into the carbon network. This conclusion is essential, as it highlights the importance of controlling the energy delivery by the power supply to the discharge.

Niu *et al*. [131] produced nitrogen-doped graphene with a nitrogen content close to 20 at.% by using a crisscross configuration of electrodes based on the principle of dielectric barrier discharges to "*suppress the excessive energy in the reaction field*". They efficiently retained graphitic N in the in-plane carbon lattice by using a mixture of pyridine and N, N-dimethylformamide (DMF). This was also true for 2-cyanopyridine/DMF and 2-aminopyridine/DMF mixtures with retention levels higher than 15%. The way energy is transferred from the electric field to the plasma and, subsequently, from electrons to the medium controls the way bonds of given precursors are broken, and free-radical polymerization processes occur. In this sense, discharges in liquids behave similarly to discharges used for plasma polymerization.

Therefore, a better understanding of the reaction pathways driven by radicals in liquids is needed. To the best of our knowledge, no attempt based on Yasuda's factor has been made yet [132].

Niu *et al*. [133] suggest another approach based on the assumption that plasma can act similarly to semiconductors. They proposed an energy band diagram of the plasma–solution junction. According to the model, the Fermi level of the selected organic molecule determines the magnitude of the electron temperature in the plasma. Benzene produced the highest electron temperature, followed by phenol, toluene, and aniline.

Finally, other functional groups could be grafted by discharges in liquids:

- −COOH, −OH and $-SO_3H$ [64]
- −S [45]
- −P [39]
- −O [62, 74]
- −B [29, 43]
- −F [29].

Process conditions

Gas bubbling

In general, gas bubbling reduces the liquid density locally within the interelectrode gap, and thereby lowers the breakdown voltage. It also promotes stirring of the solution and enhances heat and mass transfer.

Horiguchi *et al*. [122] produced platinum nanoparticles through electrode erosion and found that the presence of microbubbles created with a generator in the liquid, stabilized the discharge emission, resulting in a steady occurrence of the discharge and a lower emission intensity. Kim *et al*. [134] synthesized silver nanoobjects using a similar process and studied the influence of three different kinds of bubbles. They discovered that when very tiny bubbles were generated between the two electrodes or when only the grounded electrode was enveloped with large gas bubbles, spherical Ag nanoparticles were synthesized. However, when both electrodes were completely enveloped with large gas bubbles, Ag nanoplates were synthesized, and the discharge occurred within the gas bubbles. This partly explains the change in the growth mode of silver nanoobjects.

To remove dissolved gases from the solution, Romero Valenzuela *et al*. [65] used Ar bubbling for 1 minute before processing. However, gas bubbling is also used to better control reduction and/or polymerization processes in a given electrolyte.

Injecting gas around or through the electrodes is a way to limit the thermal vaporization of the liquid phase, which suppresses discharge instability and promotes low-temperature polymerization processes in a monomer-containing liquid [35]. The gas cools the liquid and facilitates the generation of the discharge, but in pin-to-pin configuration, this may lead to more energetic discharges that can easily carbonize polymeric particles. To control the deposited energy, pin-to-plate configuration and asymmetric bipolar pulsed voltages can be used. Optical emission spectra suggest that the discharge in this work is an argon discharge, and the active species in the liquid originate from the interface reactions that transfer electrons and active species from the gas to the liquid. This process, presented as a solution plasma, is closer to a plasma-electrochemistry process.

Pitchaimuthu *et al.* [61] used nitrogen gas to generate bubbles at the cathode in the interelectrode gap to facilitate the interaction between particles added beforehand to water and the hydrogen free-radical species created in the discharge. N_2 bubbling is more efficient than simply stirring the liquid, likely because H^{+*} species are transported farther into the liquid by the gas bubbles. The role of nitrogen in the discharge itself, assumed to be mainly composed of H- and OH-excited species from water, is not considered.

The synchronization of discharges and bubbles is a crucial factor in these approaches. In micro-gaps where high voltages are applied, breakdown can occur in either medium. If the flow of bubbles is not synchronized with discharge pulses, their role is limited to simply stirring the liquid. However, if they are synchronized, the process resembles a discharge in contact with liquid, which is a much simpler way to process a liquid.

The lack of synchronization between bubbles and discharges might be the reason for bimodal distributions of nanoparticles. This is suggested by Xing's work [76] where a high nitrogen gas flow (1 L min^{-1}) is used. At short times, two populations of sizes (centered around 5 and 50 nm) are found. On the contrary, Jang *et*

al. [35], with an argon flowrate 10 times smaller, showed large but uniform distributions. Other works do not provide sufficiently accurate statistics to draw conclusions.

One important aspect of adding a gas flow is the modification of the contamination level by elements from the electrodes of the particles produced by electrolyte reduction. According to Shin *et al.* [68], electrode erosion is reduced in the presence of bubbles, and the presence of metallic elements is also limited. This conclusion is exactly in contrast to what is stated by [35] (see above). Similar to these authors, who studied the polymerization of polypyrrole, Shin *et al*. studied a polymerization process in a solution of aniline. The former statement does not account for the possible dilution effect of impurities by larger amounts of polymerized species when bubbles are present (**Fig. 8**). Jang *et al.* assume that electrical characteristics such as current density and applied voltage are the same with or without bubbles, which is unlikely and does not correlate with Shin's electrical data reported in [69]. As argon is introduced, the voltage decreases (from 2 kV without bubbling to about 1.4 kV with 100 sccm Ar) and the current increases. It is also important to mention that these features vary with time – the discharge current decreases with time and the voltage increases – due to the synthesis of nanoobjects and modification of the solution properties (viscosity, conductivity, temperature, etc.). In any event, following Jang's reasoning, if the discharge is more energetic, electrode erosion is stronger, but polyaniline particles are likely denser. So, the contamination level changes, which probably depends on the current density in either situation as it affects both surface and in-liquid processes simultaneously.

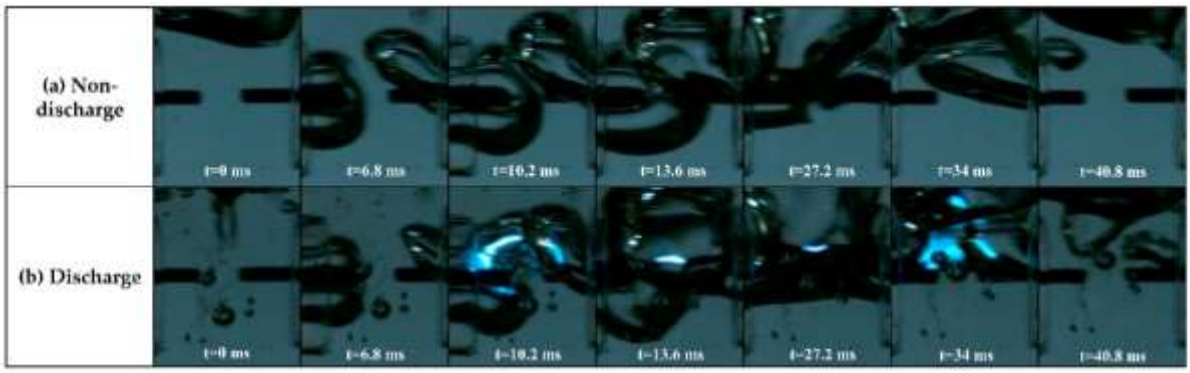

Fig. 8 Changes in the gas bubble in (a) a non-discharge case without applying a rectangular bipolar pulse, and in (b) a discharge case with applying a rectangular bipolar pulse relative to solution plasma process time. These images were obtained by high speed camera with 5000 fps and exposure time of 197 μs. After Shin *et al*. (2019) Polymers 11:105. Reproduced with permission from MDPI.

Jung *et al*. [37] found that increasing the argon flow rate from 100 to 150 sccm does not significantly affect the crystallinity of PANI particles after 50 min. Pitchaimuthu *et al*. [61] demonstrated the benefits of discharges in liquids in the presence of nitrogen gas (200 sccm) for inducing defects in a crystallized phase like TiO_2. They associate the possibility of crystal amorphization with the removal of oxygen atoms from the lattice by reacting with hydrogen excited species created in the discharge. Although they used much longer treatments (up to 15 hours), if defect creation relies on chemical processes, it is not efficient for a particle formed in the discharge conditions where the created bonds are necessarily stable unless experimental conditions change. The role of ions is deemed negligible due to the lack of energy in these media, where pressures are high. Therefore, the term "plasma-solution *sputtering*", sometimes encountered, is clearly misleading. As shown by Bratescu *et al*. [129], with the excitation energy of electrons below 1 eV in benzene and even with electrons in the tail of the energy distribution below 10 eV, it is far from the minimum of 40 eV needed to sputter tungsten [135], whereas this element can be melted by a discharge at ~0.3 eV.

Finally, Ahmadi *et al*. [136] used a nitrogen gas flow during processing by solution plasma to deoxygenate deionized water and preserve iron nanoparticles produced by electrode erosion from oxidation.

Electrical parameters

Comparison of discharges

Glow-discharge electrolysis involves the use of low voltages (typically from 50 to 500 V) and large interelectrode gap distances (> 1 cm), where the liquid functions as a conductor connecting the two electrodes. When evolution reactions create an insulating gas sheath around one electrode, discharges form and create a shortcut in the electrical circuit. Typically, currents range from 0.1 to 1 A. One electrode is much smaller than the other one, usually made of platinum, and it can be biased either positively or negatively. Consequently, current density is much higher on the smaller electrode, which is not necessarily the case in other discharge-assisted processes, such as arc discharges submerged in liquids, where pin-to-plate configurations are used. Gupta [137] indicates that the electron density estimated for the cathodic plasma is 4×10^{16} to 4×10^{17} cm^{-3} and the electron temperature is ~ 1 eV.

In solution plasma processes, applied voltages are usually in the range [0.5-2.5 kV], with interelectrode gap distances between 0.2 and 2 mm. Typically, currents from 1 to 5 A are needed to produce nanoparticles by electrode erosion, but they must be much lower (from a few tens of µA to a few tens of mA) for polymerization processes from monomer precursors in solution. Both electrodes are wires (typically 1 mm in diameter) in a pin-to-pin configuration.

The current density, rather than the current, plays a key role in the way electrodes erode and precursors in electrolytes decompose to form nanoparticles. However, determining this quantity is very challenging. Covering part of the electrodes with an insulating material, such as ceramic, glass, silicon, or butyl rubber [58, 138]), is often used to define the surface areas of the electrodes accessible to charges, which sets the current density without discharge. In the presence of discharges, the current density is determined by the contact area between the discharge channel and the electrode. Discharges are pulsed and associated with current pikes in time-current characteristics, even with “continuous” DC generators.

Submerged arc discharges require higher voltages (beyond 5 kV) and shorter gap distances (0.2-2 mm) because the liquids used in processes are more insulating than those used for solution plasmas. As a result, they are associated with “high [excitation] temperature” [2]. However, Belmonte *et al*. [139] have shown that the electron density in this kind of discharge is approximately 1×10^{17} cm^{-3}, and the electron temperature is around 1 eV. For such a heavy element as bismuth, the electron temperature can be even lower (T_e ~ 0.35 eV) [140].

Bratescu *et al*. [129] conducted spectrochemical analyses by absorption through solution plasmas run in organic solvents (benzene, pyridine, and aniline). They could determine the number density of different radicals in their ground state, such as C_2 and CN, and obtained densities close to a tenth of the electron density (~10^{17} cm^{-3}). At such a high electron density, with an estimated electron temperature of 0.6 eV by the authors, Saha’s equation is fully satisfied if the ionization energy is higher than 7.5 eV (which is ~12.6 eV for gaseous water and 8 eV for tungsten). The discharge parameters are then very similar to those of an arc discharge (**Fig. 9**). The currents, in the ampere range, oscillate at high frequency (in the MHz range). However, if the discharge is close to equilibrium, it does not necessarily mean that nanoparticles are also close to equilibrium, as their formation can occur in regions with large gradients.

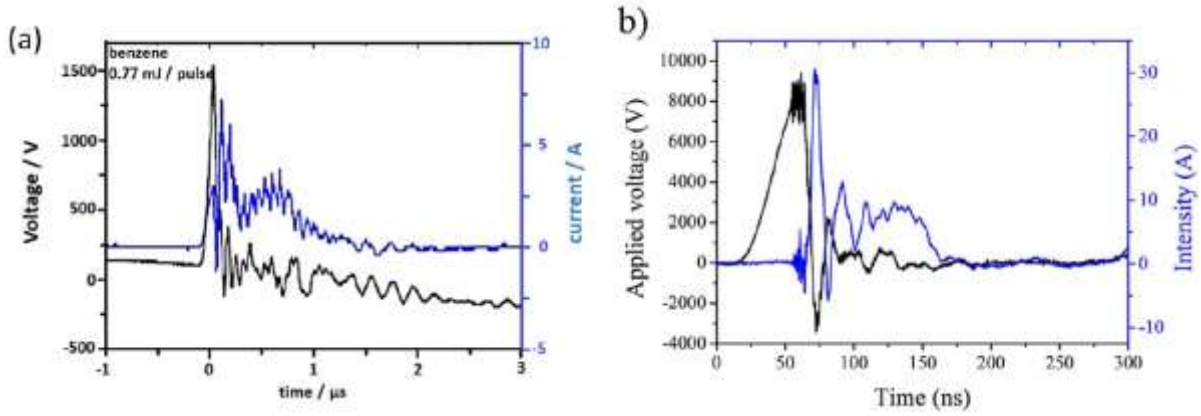

Fig. 9 Comparison between voltage and current waveforms of positive pulses in two different liquids (note that the time scales are not the same). (a) Benzene. After Bratescu *et al*. (2019) Plasma Process Polym. 16:e1900012. Reproduced with permission from WILEY-VCH Verlag GmbH. b) Liquid nitrogen. After Hamdan *et al*. (2018) Particuology 11:105. Reproduced with permission from Elsevier.

It can be concluded that the three types of discharges mentioned above, while seemingly different, actually behave similarly. It is therefore somewhat arbitrary to categorize them in this way. All three types of discharges have electron densities around 10^{17} cm^{-3} and electron temperatures close to 1 eV, and their main differences lie in the amount of energy deposited in each discharge event. Some of this energy is used to erode the electrodes, some is used to transform the liquid surrounding the discharge, and the rest is used to produce the discharge itself. It is also likely that pressure at ignition increases with the applied voltage and the electrical resistivity, with atmospheric pressure for glow discharge electrolysis exceeding typically 10 bars for submerged arcs in dielectric liquids [140] and probably in between for solution plasmas.

Shape of signals

Lee *et al*. [101] argue that the use of bipolar pulses results in more "stable" operating conditions. This excitation mode is used for symmetrical discharge generation and immediate cleaning of the tips of the two electrodes of any possible products. It is difficult to understand what Chokradjaroen *et al*. [14] meant by stating that "the bipolar pulsed power supply is key, which can help avoid raising the temperature and keep plasma to be the nonequilibrium plasma". Both temperature and shift from equilibrium are actually correlated with the current density of the discharge rather than the shape of the voltage pulse. In that sense, it is likely that polarity inversion helps to remove any remaining surface charges from electrodes from one period to another. This prevents charges from accumulating on surfaces, thus not affecting initial conditions and making the discharge process more reproducible.

Park *et al.* [57] used a ballast resistor of 1 kΩ in their electrical circuit and observed improved stability of the discharge. They inferred that the resistance decreased current spikes and limited voltage fluctuation. The resulting drawback was a decrease in the overall efficiency of the process due to energy loss in Joule heating. Alternatively, Lee *et al*. [20] added a low-pass filter circuit consisting of a parallel capacitor, a variable resistor, and a variable inductor to adjust the plasma stability. With this system, plasma stability was considerably improved by eliminating energy fluctuations.

Jang *et al*. [35] applied a DC bias to the bipolar pulse, changing the mean value from zero to either positive or negative. For a negative bias, pyrrole anions were produced by reduction of pyrrole, and a polypyrrole film was deposited on the Cu tape electrode. In contrast, for a positive bias, large polypyrrole particles were formed in the liquid phase, but no deposit was found on the tungsten wire electrode.

While the off-period between positive and negative pulses certainly plays a role in the way the temperature of the liquid rises over time, increasing the pulse width of the voltage waveform increases the supply of electrical energy to the liquid [134]. Then, a longer pulse width increases the probability of creating a discharge in a gas bubble-dominant state instead of a liquid-dominant state.

Gap distance

In general, the distance between the electrodes in a discharge setup must be short enough to enable breakdown and plasma ignition at a given applied voltage. Usually, the shorter the distance, the better. However, electrode erosion increases the gap distance over time, and the discharges can stop if the gap becomes too large.

In glow discharge electrolysis, the gap distance to consider is not the distance between the electrodes, which is always "large enough". It is actually lower than the distance between one electrode and the gas-liquid interface formed by evolution reactions around this electrode. Breakdown is made possible in this sheath once the current stops flowing, which corresponds to a breakage of the electrical percolation path caused by a denser gas layer. The gap is then much smaller than the gas sheath, which is why breakdown is possible at voltages as low as 50 V, for instance [89].

Kim *et al*. [40] were able to maintain the gap distance during the process by employing a pin-to-coil configuration of electrodes. This avoids the use of a feedback loop consisting of an electrode-gap detector and an analog electronic unit as controller to permanently adjust the position of one electrode in relation to the other to set the desired gap distance, as in [141]. For example, considering a tungsten wire with a diameter of 1 mm and an erosion rate of 100 mg h^{-1}, the eroded length after 1 h is 0.9 mm (as shown in [52]). However, the coaxial alignment of pin and coil becomes crucial to operating the system for long periods of time.

According to Hu *et al*. [31], the gap distance between electrodes affects the way vapors emitted by each electrode mix and generate alloy nanoparticles. When the gap distance increases beyond 0.3 mm in the given example, Pt and Au alloy clusters are no longer formed and are replaced by unalloyed gold and platinum nanoparticles. The main question is how gold and platinum are distributed in alloys, depending on their composition (Pt/Au ratios vary from 0.48 to 1.87). These compositions lie within the miscibility gap of the macroscopic phase diagram (*i.e.,* without including the size effect). According to the nanoscopic phase diagram, onion, Janus or surface segregated structures should be formed [142].

In contrast, Pootawang *et al*. [143] used the same process, but by using unipolar instead of bipolar pulses, they showed that Pt and Ag bimetallic nanoparticles were produced without alloying, even if Pt and Ag do alloy. The gap distance was 0.5 mm. The melting temperatures of Au, Ag and Pt are 1337 K, 1235 K and 2041 K, respectively. So, it is unlikely that alloying or not is ruled by differences in melting temperatures, as suggested by [144, 145]. It is more likely that the gap distance is too large to enable alloying. The possibility of limiting alloying by using unipolar instead of bipolar pulses is not mentioned.

Hamdan *et al*. [146, 147] used another strategy to control the discharge and the interelectrode gap distance. They created the discharge at the interface of two immiscible liquids: heptane in contact with water in [146] (**Fig. 10**) and cyclohexane in contact with a conductive solution made of Ni-nitrate and/or Fe-nitrate and/or Co-nitrate in [147]. They were able to synthesize nanoalloys of Ni-Fe, Ni-Co, Co-Fe, and Ni-Co-Fe, individually embedded in a C-matrix, with average diameters <10 nm.

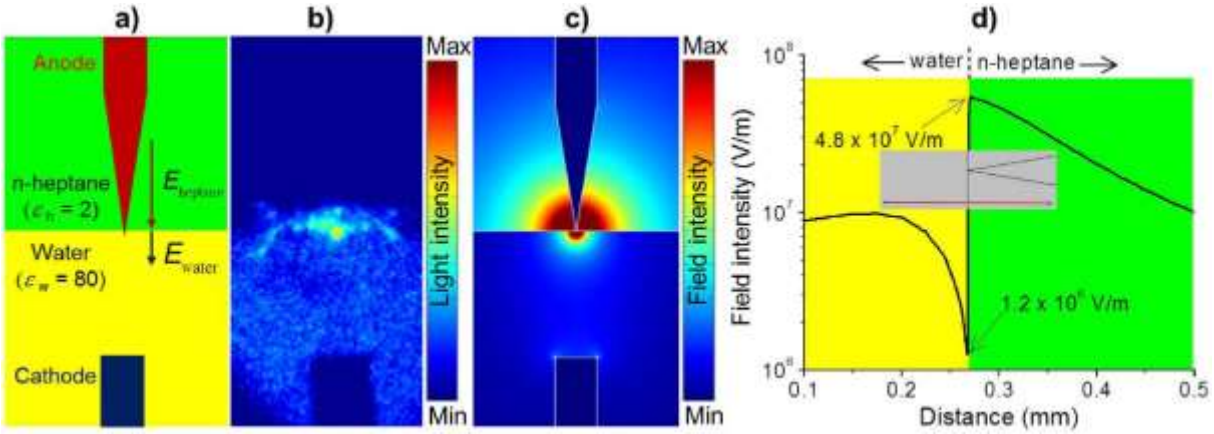

Fig. 10 a) Schematic of the experimental setup (not drawn to scale) showing the anode, the cathode, n-heptane, water, and the interface. b) ICCD image (integrated over 1 μs) of the discharge at the interface n-heptane-water (15 kV of applied voltage and 2 mm of gap distance). c) 2D electric field simulation using Comsol Multiphysics for conditions similar to b). d) Electric field profile along a line (the red line in the inset) crossing the interface close to the anode. After Hamdan *et al*. (2018) J Phys D: Appl Phys 51:244003. Reproduced with permission from the Institute of Physics.

Electrodes

Refractory metals, particularly tungsten, are used as electrodes when nanoobjects are produced by solution reduction, as electrode erosion can introduce impurities in the process by-products. Conversely, selected metals are used as electrodes if their erosion is the source of the synthesized nanoobjects. The electrodes can also be hollow to allow a gas to be blown within the interelectrode spacing. In glow-discharge electrolysis, the electrodes have unbalanced immersed areas to limit the current density on the larger electrode.

Nanoobjects production by electrode erosion is usually achieved with wires. The higher the radius of curvature, the lower the breakdown voltage. However, as electrode erosion proceeds, the radius of curvature of a pin-shaped electrode decreases rapidly and becomes too large to affect the breakdown voltage. Conversely, a too sharp electrode is consumed very quickly and limits the process yield. Wires with a diameter of 1 mm are usually used, as they provide a good trade-off between the two former limitations.

Tungsten is usually preferred as a refractory material to limit electrode erosion in solution plasma, where nanoobjects are generated by electrolyte reduction. However, discharges are often strong enough to erode tungsten and introduce this element as an unwanted trace contamination. Tantalum (melting point: 3290 K *vs.* 3695 K for W) was also tested [14], but breakdown occurs at higher energy.

Wires are often covered with isolated segments of ceramic (*e.g.,* mullite or glass) [49, 63]. This reduces the conductive area of the electrode and increases the current density. As explained by Saito *et al*. [148], anodic dissolution can contribute to electrode erosion during off-plasma periods. Due to the instabilities of the solution plasma process, electrode areas in contact with the electrolyte can be subjected to current flows. Metal ions are then released from the anode and neutralized. Atoms can then nucleate and contribute to the generation of clusters.

Using hollow electrodes is also interesting. Shin *et al*. [68] explain that obtaining polymer nanoparticles of uniform size is difficult due to the small contact surface area between the discharge and the electrolyte. Polymer nanoparticles with uniform size distributions can be produced by creating a channel of gas bubbles blown through one hollow electrode in order to increase the contact surface area and produce a stable discharge during the electrochemical plasma synthesis.

In glow-discharge electrolysis, a large platinum anode is often used with a wire cathode made of the metal to be eroded. Platinum is chosen for its chemical inertness and with large surface areas to reduce the current density. However, the opposite approach can also be taken. Yu *et al*. [93] used a large nickel anode with a platinum needle. In this case, the discharge is generated at the Pt tip. This creates OH^- ions that react with $NiCl_4^{2-}$ ions formed by cathodic dissolution to produce $Ni(OH)_2$ and Cl^-. The erosion of the Pt electrode is negligible if the applied voltage does not exceed a threshold of about 450 V.

Using alloy electrodes is also useful for generating directly alloyed nanoparticles [95]. The composition of the nanoparticles is usually slightly different from that of the eroded electrode, as some elements tend to evaporate faster than others. The compositional analysis of the eutectic Sn–35%Pb nanoparticles prepared by glow-discharge electrolysis showed the coexistence of Pb-rich and Sn-rich phases. The authors note that the uniformity of the alloy composition depends on the grain size of the electrode; smaller grain sizes promote the formation of nanoparticles with uniform compositions.

Stirring

Typically, stirring is used to homogenize the concentrations of species in the solution, disperse produced particles, and ensure uniform temperature distributions.

The stirring speed usually varies from 200 to 1000 rpm (See Table 1). Like sonication, stirring can contribute to degassing the solution.

The mode of stirring was evaluated in a work where the plasma was in contact with the solution [149]. Without stirring, the average diameter of the synthesized Au nanoparticles was around 21–22 nm in the selected conditions, and it was independent of the processing time. With magnetic stirring, the size distribution of Au nanoparticles is almost the same, with an average diameter around 22–24 nm. However, the distribution becomes narrower (from about 9 to about 7 nm). With ultrasound stirring, the average size strongly varies with time, decreasing from 75 nm (after 3 min) to 34 nm (after 10 min) with broad distributions. It is proposed that ultrasounds can increase the surface energy of nanoparticles and induce the generation of larger nanoparticles from the beginning of the process. Similar effects can be expected for discharges in liquids.

Temperature of solutions

The temperature of solutions has a significant impact on reaction kinetics in the liquid phase. Low temperatures can limit liquid evaporation, while high temperatures promote the generation of bubbles and facilitate the formation of discharges.

Oruncak *et al.* [54] demonstrated how gradually increasing the voltage from 0.1 to 0.5 and 1.2 kV to raise the temperature of water and dissipate energy by Joule heating can promote the formation of discharges. Evaporation of water begins only at 0.5 kV, forming small bubbles, but no discharge. Discharges begin to appear beyond 1.6 kV. This approach is preferably used for large electrode surface areas [150, 151] with liquid temperature being regulated close to the boiling point. This is why temperatures are usually higher in glow discharge electrolysis than in solution plasma.

In contrast, Che *et al*. [27] and Huang *et al*. [32] set the temperature of water at 10 °C. Cooling the solution is claimed to be a way to avoid introducing bulk defects in materials post-treated by solution plasma at high temperatures. As the authors used nitrogen flow assistance through one hollow electrode (W, 3 mm in diameter), we assume that cooling the liquid to this temperature also strongly limits the presence of water inside nitrogen gas. This might limit oxidation and promote reduction processes.

Samimi-Sedeh *et al*. [90] investigated the effect of liquid bath temperature on the synthesis of Na_2FeO_4 nanoparticles via glow discharge electrolysis with low AC voltage. They used a carbon steel wire as anode

in water containing NaOH. The temperature increased during the process, with an amplitude that depended on the initial temperature selected in the range from 5 to 45°C. After 5 min, for an initial temperature of 5°C, the final temperature was 25°C, and 39°C for an initial temperature of 35°C. The incubation time awaited before discharge ignition varied from 186 s at 15°C to 1 s at 45°C. The maximum production of nanoparticles was achieved at an initial temperature of 30°C. The existence of this maximum production is attributed to a change in reaction pathways in the electrolyte.

This phenomenon has also been observed in other works using gelatin [115, 116]. Cross-linking reactions occur at 22 °C, while depolymerization is observed at 40 °C. Therefore, changing the liquid temperature can influence reactions if transitions in pathways exist at temperatures remaining below the boiling point of the liquid.

In the case of cellulose processed in highly concentrated sulfuric acid, Surov *et al*. [111] explain that higher temperatures usually lead to higher surface charges and narrow particle size distributions, but lower yields and decreased crystallinity and thermal stability of nanocrystals.

Che *et al*. [27] suggest that because the "thermal conductivity of liquids is much higher than gases, defects can be mildly introduced by solution plasma (contrary to gaseous processes), ensuring the selective introduction of defects on the surface of oxides". This assertion implies that heat transfer between the particles and the liquid is controlled by the thermal conductivity of the liquid phase. However, this is only true if the particle temperature is lower than the liquid's boiling point. Beyond this limit, a gas phase forms around the particle, and heat transfer is controlled by the thermal conductivity of the gas phase. In other words, the previous assertion assumes that defects are created by the reaction of particles with species created by the plasma in the liquid phase, which is yet to be demonstrated.

Time

Treatment time

The treatment time plays a strategic role in the processing of nanoobjects in liquids. It is always correlated with the reactor design (material, volume, overflow, stirring,…), which affects the residence time, and the liquid composition, which defines the kinetic rates for given discharge conditions. Treatment time varies from minutes to hours. In general, short times are preferred for the synthesis of small nanoobjects, as the mean size usually increases via in-liquid growth and agglomeration [143].

The same authors [152] showed that sufficiently long treatment times (> 3min in the selected condition) are needed to avoid undesirable oxidation reactions of copper nanoparticles in the presence of gelatin as capping agent. This was attributed to a reduction of particle size and a change in morphology (from spherical to anisotropic), together with the adsorption of the capping agent during particle growth.

Long treatment times are needed for high throughput production, and increasing the treatment time usually modifies size distributions. In a non-thermostatic bath, liquids are heated up by the energy released during the discharge process. Elevation of temperature beyond 30 °C typically affects significantly the kinetics of the agglomeration process [153], leading to a broadening of the size distribution due to bimodal growth. Yoshida *et al*. [81] produced Ag nanoparticles by electrode erosion and observed a significant change in the size distribution from 75 s to 600 s, varying from [3.0-20] nm to multimodal [3.0-58] nm (**Fig. 11**). Such a change was attributed to Ostwald ripening, likely enhanced by temperature, as the process was not regulated in temperature. As observed by Pootawang *et al.* [143], the increase in the temperature of the solution as time passes results in faster growth. As size increases, the surface/volume ratio of the particles decreases, affecting their zeta potential and their stability in the solution, promoting agglomeration. For these reasons, cooling the liquids or using continuous flow processes [122] is a way to reduce agglomeration processes.

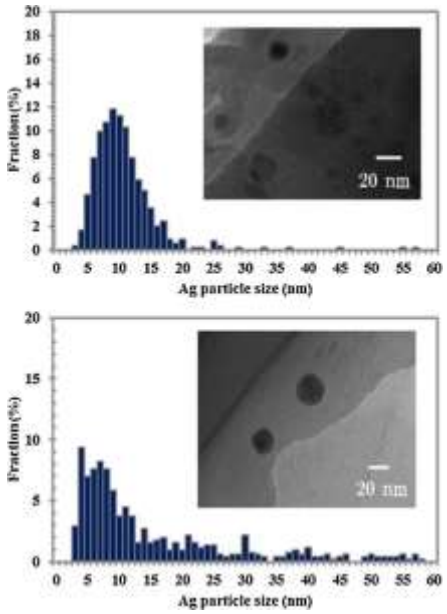

Fig. 11 TEM images and size distribution histograms of Ag nanoparticles obtained after 75 s (upper) and 600 s (lower). After Yoshida *et al*. (2018) Catalysis Today 303:320. Reproduced with permission from Elsevier.

Long treatment times can also narrow size distributions and even decrease the mean size under certain conditions. According to Jiang *et al*. [153], a fusion growth process, different from the Ostwald ripening mechanism, can cause the decrease in particle size. This process results in the merging of a small particle with a larger one, which usually increases the size of the larger one, but in this case, it leads to a medium-sized particle, probably due to structural rearrangement [154]. This process applies to both spherical and non-spherical particles. MubarakAli *et al*. [50] produced CeO_2 spherical nanoparticles with average diameters decreasing with time, from ~7.0 nm after 15 min to ~5.0 after 25 min. However, the decrease in the average diameter with time seems to result more from limited statistics and/or samplings than from physical reasons.

The shape of nanoparticles can drastically change with treatment time if experimental conditions (pH, temperature, liquid composition, conductivity, etc.) drift significantly. Kim *et al.* [134] attributed the change in the shape of silver nanoparticles to the synthesis mechanism, which varies according to the way the discharge bubble forms. The pulse width could be modified from 20 to 60 μs in water heated at 80 °C to enhance bubble formation and facilitate breakdown. The way the bubble forms results from the characteristics of the discharge. Lee *et al*. [104] demonstrated how the increase of the interelectrode gap distance (from 0.25 to 1 mm) in a benzene solution affects the structures and the H/C ratios of the produced nanocarbons. Therefore, keeping the gap distance constant as electrodes erode with time is crucial to preserving the characteristics of the synthesized nanocarbons. It is thus essential to keep discharge parameters as constant as possible. Kim *et al*. [40] produced ZnO nanobullets by using a zinc coil as the electrode in water. They suggest that the specific shape of particles results from the discharge created with the chosen arrangement, which overcomes the discharge interruption. Kim *et al*. [41] also studied the synthesis of ZnO nanostructures by discharges in water mixed with zinc nitrate hexahydrate and hexamethylenetetramine. Nanorods or nanosheets were formed depending on whether one electrode was made of W or Zn. WO_4^{2-} ions, released progressively by electrode erosion, inhibit growth in the [001] direction, which affects the general shape.

It is a valid question to ask whether the shape of nanoparticles remains unchanged when experimental parameters are held constant. Chemical processes have shown that nanoparticle shapes can be time-dependent [155]. Typically, spherical nanoparticles are observed to maintain their shape. However, Treesukkasem *et al*. [156] demonstrated significant changes in the shape of gold nanoparticles over time by reducting $HAuCl_4$,

particularly in gelatin. However, it is not clear if these changes are solely driven by kinetics, as the process temperature also evolves freely during the synthesis.

In the same study, the authors highlighted the crucial role of treatment time in determining the hydrodynamic radius of Au nanoparticles produced in solutions containing various sugars and biopolymers. Over time, gold ions generated by plasma reduction of $HAuCl_4$ assemble and grow in the natural matrix cavity (**Fig. 12**). Reactive species from the discharge interact with the carbonaceous shell and reduce their molecular weights. Consequently, the shell shrinks, and the hydrodynamic diameter of nanoparticles decreases with prolonged treatment.

Fig. 12 Schematic representation of a possible phenomenon for the hydrodynamic diameter reduction of the AuNP colloids with prolonged plasma treatment. After Treesukkasem *et al.* (2019) ACS Appl Nano Mater 2:8051−8062. Reproduced with permission from the American Chemical Society.

Liu *et al.* [46] have reported that the mass of Pt nanoparticles generated by erosion is mainly influenced by the diameter of the discharge electrodes and the discharge time, but no further details are given. Mani-Lata *et al*. [47] observed an increase in the production of platinum nanoparticles with time in a solution containing Ketjen Black (KB) particles (30-50 nm in size), but the possible effect of the presence of KB was not described.

Pootawang *et al*. [143] showed that the synthesis of platinum and silver nanoparticles leads to a linear increase in the electrical conductivity of the solution over time (0-120 min). The composition of Ag/Pt nanoalloys changed slightly over time, with an increase in the silver content from 94.65 to 96.10% based on EDX measurements. However, due to the inaccuracy of quantitative EDX measurements on small objects and elements with low concentrations (less than 5 wt.% typically, which is the case here for Ag), this evolution can be considered negligible. The larger amount of silver compared to platinum is due to the large difference in melting temperatures between the two elements [1235 K *vs.* 2041 K].

Ageing

Ageing causes changes in the solution's pH and conductivity, which affect the reactivity of chemical species or trigger post-plasma reactions, leading to degradation that continues long after the plasma treatment [8].

Chantaramethakul *et al*. [26] synthesized gold nanoparticles by electrode erosion and produced a colloidal suspension after 10 minutes of treatment. Using 0.5 mL of NaCl in water, they obtained a size distribution ranging from 2.2 to 19 nm and centered at 7.6 nm. After 15 days of ageing, the distribution evolved and was found to be [2.8-14.6] nm (centered at 6.1 nm). It changed again after 30 days to [4.8-19] nm (centered at 8.5 nm). This unusual evolution is due to the presence of gold ions ($AuCl_4^-$) in the NaCl solution containing the

particles, which form chain assemblies after processing. In the first step, these ions react with Au^0 from the particles and produce $AuCl_2^-$ ions, leading to a decrease in particle size. Next, when the etching process reaches equilibrium, the etched Au nanoparticles serve as seeds for further growth by Ostwald ripening (wherein Au^{3+} ions are converted into Au^0), resulting in larger particle sizes over an extended storage time.

Engineering of defects by post-processing

Discharges in liquids are an effective method for creating defects in nanoobjects. Tran *et al*. [157] used high-voltage discharges in a DBD configuration to gel a sol made of water, titanium tetraisopropoxide and HNO_3. Argon was bubbled into the liquid, and the synthesized mixtures of defective anatase and rutile crystals were calcinated before use. These crystals exhibited superior photocatalytic activity when compared with the pure-phase samples. Pitchaimuthu *et al*. [61] processed pure anatase commercial TiO_2 powders by solution plasma in water with nitrogen flow assistance. They formed anatase/brookite hetero-crystalline phases with oxygen vacancies through interaction with the discharge over several hours. This phase showed improved photocatalytic performance for acetaldehyde degradation to CO_2 compared to untreated TiO_2 and nitrogen-doped TiO_2. Jedsukontorn *et al*. [36] eroded a titanium electrode in a solution containing nitric acid for several hours, resulting in the formation of defective black TiO_2. Defects like Ti−H and O−H introduce mid-gap states. They change the color of pristine TiO_2 from white to blue, green, or black. Synthesized micrometric particles are made of anatase/rutile polycrystals, and their photocatalytic activity was significant when tested for glycerol conversion. Zhu *et al*. [158] also synthesized black TiO_2 through the erosion of a titanium cathode in KOH heated at 80 °C. Black H-TiO_{2-x} nanoparticles result from a hydrogen doping process in the liquid phase of TiO_{2-x} nanoparticles emitted from the oxidized surface of the titanium electrode. They are surrounded by a structurally disordered shell and exhibit superior performance in generating water vapor from liquid water under simulated solar irradiation by solar−thermal water evaporation. Yu *et al*. [159] used solution plasma to treat two-phase TiO_2 homemade nanoparticles containing anatase and another monoclinic polymorph named TiO_2(B). This heterojunction already possesses a large number of oxygen vacancies. Post-treatment by solution plasma with nitrogen flow assistance was used to introduce shallow energy levels via hydrogen doping and to fine-tune the gap between oxygen vacancies and the conduction band of TiO_2. They reported that solar photothermal catalysis over colored oxygen vacancy-rich TiO_2 is enhanced by incorporating shallow donor levels of hydrogen. Interestingly, in this case, the treatment duration did not act linearly on the performance of the catalyst. After 2 hours, hydrogen dopant at the shallow level increased, and oxygen vacancies at the deep level decreased. After 4 hours, as these evolutions continue, the content of oxygen vacancies becomes too low to maintain the photothermal catalytic activity (**Fig. 13**). The lowering of deep-level defects is attributed to the annealing process caused by the high-temperature discharge. It is not clear why the creation of oxygen vacancies in this process is not observed, as in the works by Pitchaimuthu *et al*. [61] and Jedsukontorn *et al*. [36]. It is not because of the nitrogen flow assistance, also used by the former authors, other experimental conditions being almost the same (the presence of KCl in Yu's work, Pitchaimuthu using deionized water only, is deemed not relevant here on the basis of Huang's results [32] described in the next paragraph). Then, we assumed that it was only due to the initial state of TiO_2, where the presence of deep defects in large quantities at the beginning may not permit the creation of new ones. The sizes of the objects are pretty similar: BET area of 136 $m^2\ g^{-1}$ and mean diameter of 10 nm in Yu's work, 289 $m^2\ g^{-1}$ and 5 nm in Pitchaimuthu's work. In their study, Wang et *al*. [160] opted to use solution plasma in ethanol to process commercial P25 TiO_2, rather than water. This approach offers several advantages. Firstly, because alcohol has a lower dielectric constant compared to water, it requires less power to ignite discharges. Additionally, ethanol's lower boiling point and surface tension lead to smaller bubbles between the discharge electrodes, facilitating the solution discharge process. Ethanol is also easily split into hydrogen, oxygen, and hydroxyl radicals. Hydrogen dopes more easily titanium oxide. Moreover, oxygen-containing radicals contribute to passivating oxygen vacancies. The authors found that P25 particles treated in ethanol plasma exhibited a 124-fold increase in photocatalytic H_2 evolution. This effect was attributed to the surface

amorphization, which resulted in a decrease in surface deep electron traps and an up shifted energy level of electron traps.

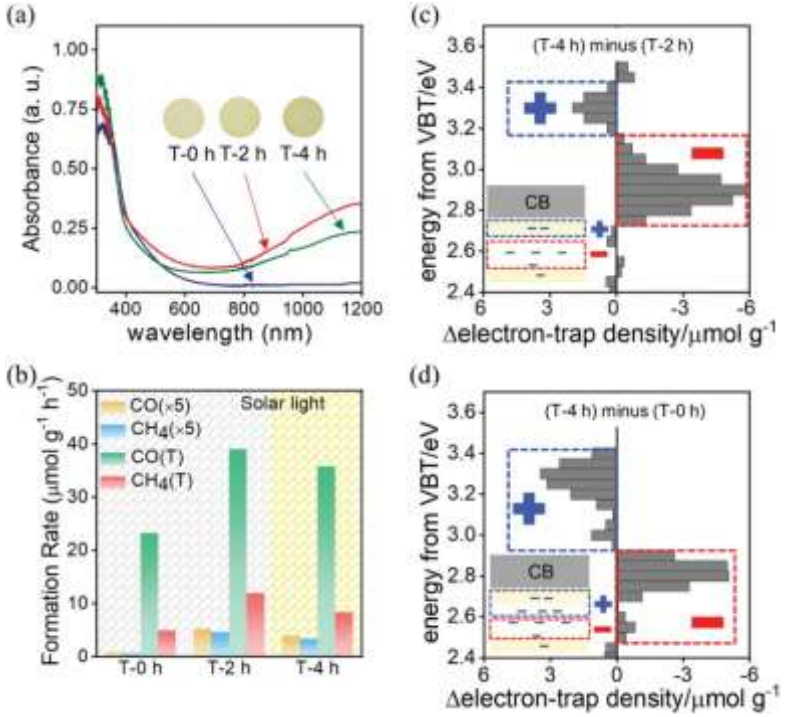

Fig. 13 a) Ultraviolet–visible absorption spectra of TiO_2(AB) treated by SPP for T-0 h, T-2 h, and T-4 h. Circles around each sample name is a photograph of the actual sample color. b) Photocatalytic and photothermal catalytic activities of CO_2 conversion over T-x upon exposure to solar light. Reversed double-beam photoacoustic spectroscopy of Δelectron-trap-density c) between T-4 h and T-2 h and d) between T-4 h and T-0 h. After Yu *et al.* (2020) Adv Sci 7:2000204. Reproduced with permission from WILEY-VCH Verlag GmbH.

Huang *et al*. [32] have proposed similar effects to those identified by Yu *et al*. [159]. They activated HNb_3O_8 nanosheets by solution plasma in ethanol to anchor carbon nanodots formed *in situ* on their activated surfaces. The authors observed that the Fermi level of HNb_3O_8 was up shifted after treatment, and may result from the introduction of shallow energy-level defects by hydrogen doping. Conversely, the top of the valence band was downshifted. The authors suggest a passivation of the defect state in the original HNb_3O_8 nanosheets, resulting from the annealing by the discharge. However, they also suggest in the same work the possible role of O^{2+} cations formed in ethanol (and not in water), which might inhibit the formation of oxygen vacancies. Decoration by carbon dots promotes electron transfer from HNb_3O_8 to the dots, enhancing photocatalysis.

With another oxide, namely $BiVO_4$ known for its capability of separating charges across exposed {0 1 0} and {1 1 0} facets, Che *et al*. [27] showed that solution plasma in water with KCl for 8 hours was efficient for introducing vanadium vacancies. This leads to electron trapping and enhanced charge separation. Although the way vanadium is taken out of the structure by discharge processes is not explained, it opens up interesting perspectives on how to selectively remove one element from an alloy.

Particles are likely reprocessed several times during the treatment, especially for long treatment durations and small liquid volumes (~100 mL), and defects can be created, like in the former work, by successive interactions with the discharge. Jedsukontorn *et al*. [36] indicate other possibilities, such as the rapid quenching of the molten Ti clusters leaving the electrode and/or the reaction between the oxygen lattice in the generated TiO_2 and species such as electrons, H, O and OH radicals inside the plasma that would create oxygen vacancies. This latter mechanism is also proposed by Zhou *et al*. [161], who formed highly-defected

WO_3 nanoparticles. Of course, this kind of interaction can occur not only during the synthesis process of the nanoparticles but also during their post-processing by the discharge once they are synthesized.

Liu *et al*. [162] used solution plasma to introduce defects in heterojunctions made of semiconductive metal–organic framework $Co_xNi_{3-x}(HITP)_2$ (HITP: 2,3,6,7,10,11-hexaiminotriphenylene) and boron nanosheets, resulting in an effective catalyst for the electrocatalytic nitrogen reduction reaction under ambient conditions. DFT calculations showed that the plasma treatment significantly enhanced the adsorption and activation of N_2 molecules on the heterojunction, thus improving the electrocatalytic nitrogen reduction reaction.

Niyitanga *et al*. [163] attributed the improved catalytic activities of thermally reduced graphite oxide-supported molybdenum disulfide ($RGO@MoS_2$) hybrids to high electrical conductivity and increased sulfur vacancies resulting from the solution plasma treatment. They also reported an increase in the active surface area of the treated materials by about a factor of 4 after 10 hours.

Glow discharge electrolysis also leads to defect-rich nanoparticles, as demonstrated by Yu *et al*. [93]. They synthesized $Ni(OH)_2$ flower-like microspheres by eroding a nickel anode for one hour in 150 mL of electrolyte with NaCl, which promotes nickel dissolution, and CH_3COONa, which acts as a stabilizer. Structural defects and disorders, such as different proton sites in a disordered structure containing H_2O and O^{2-} defects, were observed. As particles assemble through the Ostwald ripening mechanism, it is very likely that they interact with the discharge several times during processing, leading to the formation of defects. However, these defects might also be due to the formation mechanism of nuclei and/or to their assembly into larger structures.

APPLICATIONS

To demonstrate the capabilities of discharges in liquids, we have chosen four of the most widely studied applications: batteries, supercapacitors, photocatalysis, and biological applications.

Batteries

Graphite is the most commonly used anode material for lithium-ion batteries, but its low lithium-ion insertion potential (approximately 0.1 V) creates safety issues due to the potential for lithium precipitation and dendrite formation during cycling. Wei *et al*. [164] proposed using solution plasma to produce $LiEuTiO_4$ in a single step, which operates at 0.8 V as anode material without lithium precipitation or battery voltage reduction. The particles are relatively large (with an average of 160 nm), but they have a high specific surface area of about 120 $m^2\ g^{-1}$. Saito *et al*. [151] synthesized silicon nanoparticles (with a mean diameter of ~100 nm) by glow-discharge electrolysis in a liquid containing LiCl and H_3BO_3, which was then heated to ~93-95 °C. After combining the nanoparticles with carbon using MgO-template-assisted sol-gel combustion, the composite exhibited a high reversible capacity of 537 mAh g^{-1} after 30 discharge/charge cycles at a current rate of 0.5 A g^{-1}.

Kim *et al*. [39] proposed to synthesize P-doped carbon balls as anode material in sodium ion batteries using a solution plasma process. The carbon balls have disordered amorphous structures and contain up to 4 at% of phosphorus. When organized in porous architectures with meso- and macropores, they efficiently adsorb Na^+ ions while accelerating their transport properties. They exhibit a high initial coulombic efficiency of about 75% and a high reversible capacity of 340 mAh g^{-1} at a current density of 1 A g^{-1}.

Chokradjaroen *et al*. [30] and Islam *et al*. [33] investigated cathodic materials that can efficiently catalyze the oxygen reduction reaction for use in energy-conversion $Li–O_2$ batteries. The former synthesized simultaneously amorphous carbon containing boron (from tributyl-borate) and tungsten carbide (W was from the electrodes) in suspension in the liquid phase, along with graphite-like carbon, as precipitate. B-doped carbon showed an initial capacity of 6200 mAh g^{-1}, while the graphite-like carbon resulted in the formation

of Li_2O_2, and, to a lesser extent, of Li_2CO_3 and lithium acetate products upon discharge in the Li-O_2 cell. WC contributes to the efficiency of the produced material as a cathode coating material that can enhance the performance of Li–O_2 batteries. The latter produced nanocarbons from aniline with tungsten carbide (W was also from the electrodes) and obtained a capacity of 15500 mA h per gram of carbon at a discharge rate of 0.1 mA cm^{-2} with a load of 1.0 mg in carbon. Cyclic voltammetry in sulfuric acid saturated with N_2 and O_2 showed the oxygen reduction reaction of the nanocarbons, with a proposed synergistic effect between N and WC. For metal-air batteries, carbon doping by heteroatoms can tune its electronic properties and reactivity by providing more active sites and enhancing the interaction between carbon structure and active sites [43]. Li *et al*. [45] found that the stability of platinum nanoparticles loaded onto sulfur-doped nanocarbons, synthesized by solution plasma from mixtures of benzene and thioanisole, improved over longer cycles. Lee *et al*. [20, 43] came to similar conclusions with (N and/or B)-doped nanocarbons.

Controlling size distributions is a key factor in the properties of materials made of nanoobjects. For instance, it is relatively simple to produce platinum nanoparticles with diameters around or even below 5 nm [46, 47, 59, 122]. In contrast, manganese oxide nanoparticles are generally larger (between 20 and 100 nm typically) [9, 60, 91, 94]. While recipes are available, no model can predict how to set parameters to achieve the desired range of sizes.

It has been found that "impurities" like tungsten can have both positive and negative effects on the properties of composites, depending on the circumstances. However, controlling electrode erosion by discharges remains a challenge, as it is difficult to fully suppress or accurately set to a desired level. In this regard, models could be useful.

Supercapacitors

Lee *et al*. [44] synthesized Fe_3O_4 nanoparticles by solution plasma and used them to impregnate nitrogen-doped activated carbon, also synthesized by solution plasma. The specific surface area of the composite reached ~1500 m^2 g^{-1}. Similar to batteries, nitrogen doping in carbon increases charge transfer rates, and composites containing Fe_3O_4 exhibit a lower equivalent series resistance. The initial specific capacitance of composites was ~125 F g^{-1}, which decreased to ~110 F g^{-1} after 300 cycles. Yu *et al*. [92] also synthesized Fe_3O_4 nanoparticles but used glow discharge electrolysis. With mean sizes below 20 nm, these nanoparticles, used as electrode material, likely have a large surface area and exhibit a specific capacitance of 247 F g^{-1} at a current density of 0.5 A g^{-1}. Even after 5000 cycles, the nanoparticles maintain a capacity retention of 41.1%.

Xiu *et al*. [94] deposited two different Mn_3O_4 nanostructures (nano-octahedron and nanosheets) on a carbon cloth by changing the applied voltage in a glow discharge electrolysis process. The nanosheet-cloth composite delivers a better capacitive performance (488 F g^{-1}) and remarkable cycle life (10,000 cycles with 99.1% capacity retention), due to the nanoporous structure of the nanosheet, which provides a larger electrochemical active surface area (**Fig. 14**). Wang *et al*. [91] synthesized Mn_3O_4 microspheres using glow discharge electrolysis, but at higher voltages and lower currents than Xiu *et al*. The microspheres were made of an assembly of small (~20 nm) and large (~180 nm) nanospheres. The microspheres exhibited a specific capacitance of 360 F g^{-1} at 0.5 A g^{-1} and a superior cycling property with 83.6 % capacity retention after 1000 cycles at 1 A g^{-1}. The specific area of the nanospheres was ~48 m^2 g^{-1}, which is probably smaller than that of Mn_3O_4 nanosheets. Pimklang *et al*. [60] elaborated a graphene oxide-MnO_2 nanocomposite and measured a specific capacitance of 218 F g^{-1} within an aqueous environment. The composite exhibited a capacity retention of 85% after 1000 cycles.

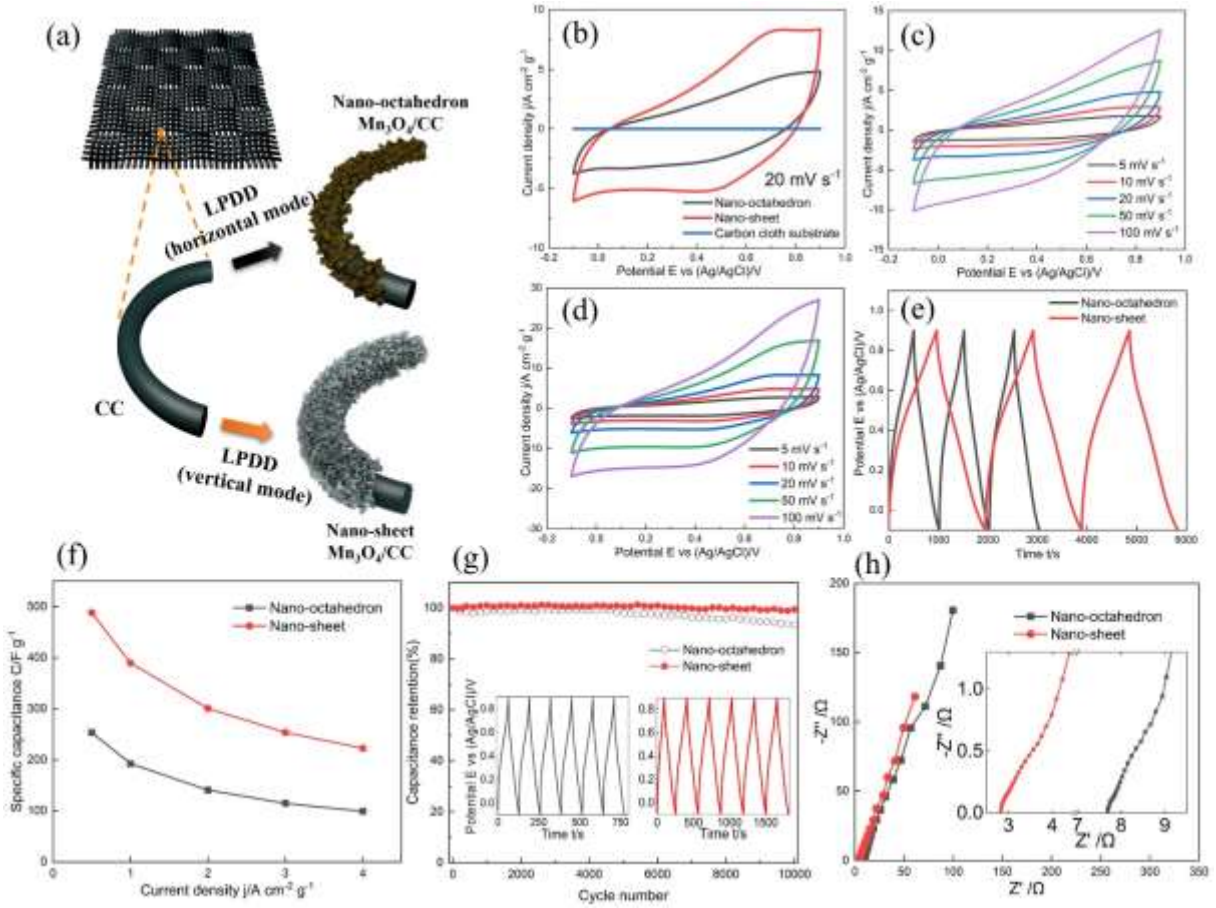

Fig. 14 (a) Schematic illustrating liquid plasma discharge deposition (LPDD) processing of nano-octahedron and nano-sheet Mn_3O_4/carbon cloth composites; (b) CV curves of nano-octahedron and nanosheet Mn_3O_4/carbon cloth composites, and bare carbon cloth substrates under scan rates of 20 mV s^{-1}; (c) CV curves of nano-octahedron Mn_3O_4/carbon cloth composites, and (d) nano-sheet Mn_3O_4/carbon cloth composites at different scan rates; (e) Galvanostatic charge discharge curves at a current density of 0.5 A g^{-1}; (f) Calculated specific capacitance at different current densities; (g) cycle stability tests at a current density of 2 A g^{-1}, the inset shows the galvanostatic charge discharge curves of the last 6 cycles; (h) Nyquist plots of the nano-octahedron and the nano-sheet Mn_3O_4/carbon cloth composites, the insert shows the Nyquist plots at high frequency region. After Xiu *et al.* (2023) Electrochim Acta 439:141620. Reproduced with permission from Elsevier.

Yu *et al*. [93] used cathode glow discharge electrolysis to erode nickel electrodes and fabricate 3D flower-like β-$Ni(OH)_2$ microspheres. These microspheres exhibit a high specific capacitance of 1818 F g^{-1} at 3 A g^{-1} and good capacity retention of 85 % after 1000 charge–discharge cycles at a current density of 5 A g^{-1}.

These studies emphasize the importance of synthesizing non-spherical particles using discharges in liquids. They demonstrate the advantage of mastering the process conditions and electric fields to design shapes that are well-suited to the application. While using electric fields to assemble nanoparticles into 1D nanostructures is well understood [85] and mastered [165], controlling porosity and defects is challenging as it relies on processes that are very difficult to control. Additionally, selecting the thickness of 2D objects produced by discharges in liquids is complicated. A better understanding of how these objects are produced is necessary to improve their design.

Photocatalysis

Photoactive nanoparticles have shown potential for use in water splitting [27, 47, 166]. Che *et al*. [27] utilized solution plasma to mildly introduce defects for surface activation of decahedral $BiVO_4$ crystals. This technique enhanced the oxygen reduction rate (ORR) from water oxidation under visible light by a factor of 1.5. Similarly, Panomsuwan *et al*. [56] improved the ORR by using a composite consisting of silver nanoparticles supported on nitrogen-doped carbons created via solution plasma. They achieved this by utilizing two electrodes of silver immersed in 2-cyanopyridine ($C_6H_4N_2$), taking advantage of the synergistic effect of Ag nanoparticles and NC nitrogen-doped carbon supports.

In another study, Mani-Lata *et al.* [47] proposed architectured nanomaterials composed of platinum nanoparticles supported on Ketjen Black (KB) to improve evolution reactions in water splitting. Solution plasma was used to improve adhesion between the nanoparticles and the dispersed carbon in comparison to a similar commercial catalyst. This better anchorage was deemed responsible for the improvement of the activity and stability of both the hydrogen evolution reaction (HER) and ORR.

Islam *et al*. [34, 167] synthesized tungsten carbide/carbon nanocomposites (C coming from palm oil and W from electrodes), and enhanced the activity of the oxidation reduction reaction in alkaline solution for fuel cell application. With a surface area of 160 $m^2\ g^{-1}$, the WC/C nanocomposites reached an electrical conductivity of 4.27×10^{-2} S cm^{-1}, which is ~5 times higher than that of Ketjen Black.

Cui *et al*. [166] used solution plasma to load bimetallic oxide alloy nanoparticles made of Pt and Pd onto exfoliated two-dimensional MXene ($Ti_3C_2T_x$, where T is a functional group, here synthesized from Ti_3AlC_2 where Al was removed by HF and functionalized next in dimethyl sulfoxide). They measured a low overpotential for the HER (57 mV) in a 0.5 M H_2SO_4 solution and for the ORR (1.63 V) in 0.1 M KOH solution. They could achieve a water splitting current density of 10 mA cm^{-2} at 1.53 V in a 1.0 M KOH solution. For comparison, Niyitanga *et al*. [168] created surface defects in MoS_2 nanosheets using the solution plasma process and measured HER and ORR overpotentials of −0.06 V and 1.22 V with a current density of 10 mA cm^{-2}.

Using bimetallic nanoparticles is a way to improve the efficiency of a water splitting cell. The synthesis of Au-M bimetallic particles (where M is another metal) was studied by Bratescu et al. [148, 169]. ***Table 3*** *shows the nanoparticles synthesized from different metal precursors. Gold-containing bimetallic nanoparticles exhibited sizes in the range from 5 to 20 nm. The gold content was high in alloys with a 3d metal, and the difference in electronegativity between gold and the other metal was responsible for the formation of intermetallic compounds. It can be noticed that the composition of gold-cobalt nanoalloys is not compatible with the macroscopic equilibrium phase diagram, which suggests that non-equilibrium phases are synthesized with the solution plasma. It is also true for Pt and Pd as reported in detail in another work by Zhang et al. [170]. The possibility of using non-equilibrium multi-metallic nanoalloys is a strong expectation of such processes [171], in order to evaluate their potentiality as a new class of materials in applications where temperature ranges are compatible with their utilization, such as water splitting.*

Au-M	Composition from RIR method[a]		Average size (nm)		Morphology aggregation solubility in water
	Gold (wt%)	Other compounds (wt%)			
Divalent sp metals					
Au–Zn	48	$Zn(OH)_2$	46	20	Chains of NPs which tend to aggregate
		Au_3Zn	5		
		$Zn_{0.965}Au_{0.035}$	1		Insoluble
Au–Cd	63	AuCd	10	20	Chains of NPs which tend to aggregate
		$Au_3Cd_{2.97}$	27		Insoluble
Trivalent sp metals					
Au–Ga	3	$(Au_{23}Ga_2)_{0.16}$	37	5	Sphere
		$Au_{0.9}Ga_{0.1}$	3		No aggregation
		$(Au_9Ga)_{0.4}$	57		Soluble
Au–In	69	$(Au_{23}In_2)_{0.16}$	31	3	Sphere
					No aggregation
					Soluble
3d Metals					
Au–Fe	85	$Au_{0.05}Fe_{0.95}$	15	5	Almost no aggregation
					Slightly soluble
Au–Co	78	$(Au_9Co)_{0.4}$	5	10	Chains of NPs which tend to aggregate
		Au_4Co	16		
		$Co_{0.975}Au_{0.025}$	1		Insoluble
Au–Ni	95	$Ni_{0.92}Au_{0.08}$	1	10	Chains of NPs which trend to aggregate
		$Au_{0.45}Ni_{0.55}$	4		Insoluble
Au–Cu	80	Au_3Cu	3	10	Chains of NPs which tend to aggregate
		$Au_{0.8}Cu_{0.2}$	4		
		Cu_2O	13		Insoluble
4d Metals					
Au–Ag	29	Ag	26	8	Sphere
		AgAu	45		No aggregation.
					Soluble
Au–Pd	73	AuPd	8	8	Chains of NPs which tend to aggregate
		$Au1.1Pd_{0.9}$	8		
		$(AuPd_9)_{0.4}$	10		Soluble
		$Pd(NO_3)_2$	1		

[a] The gold bimetallic NPs were prepared from a solution with an initial salt concentration of 1 mM.

Table 3 Composition, size, morphology, and water solubility of gold bimetallic nanoparticles synthesized in SPP. After Bratescu et al. (2013) J Alloys Compounds 562:74–83. Reproduced with permission from Elsevier.

Photoactive nanoparticles can also be used for the degradation of chemicals. Defective structures exhibit high capabilities in this objective, as discharges in liquids provide a promising platform to tailor the surface microstructure of catalytic materials.

Zhou *et al*. [161] synthesized WO_3 nanoparticles to enhance photooxidation of bisphenol A by persulfate by about one order of magnitude. They discovered that the interaction of hydrogen species with the surface of the catalyst generated abundant oxygen vacancies. The synergistic effect between WO_3 and persulfate was attributed to defect sites and intercalated hydrogen, which facilitate the formation of surface-bridging hydroxide via surface hydroxylation. This provides specific channels for electron and hole transfer, resulting in significantly increased efficiency for pollutant elimination.

Sirotkin *et al*. [71, 172, 173] also synthesized WO_3 nanoparticles and studied the photodestruction of the dye rhodamine B in aqueous solutions under the action of UV radiation with and without the synthesized tungsten oxide powder. They attributed the high photocatalytic activity of WO_3 nanoparticles to the low values of the band gap and the porous structure of the sample.

The photocatalytic performance of silver-loaded gallium oxide (Ag/Ga_2O_3) photocatalysts was evaluated by Yoshida *et al*. [81]. The presence of silver nanoparticles, synthesized by solution plasma and loaded onto Ga_2O_3 powders, could strongly improve the photocatalytic reduction of CO_2, but they also observed that the CO production rates decreased with the reaction time. As silver nanoparticles migrate and aggregate on the photocatalyst surface during the photocatalytic process, their global efficiency decreases. Photoirradiation on the prepared Ag/Ga_2O_3 samples improves the photocatalytic performance, likely by introducing defects.

Pitchaimuthu *et al*. [61] utilized solution plasma to synthesize heterocrystalline anatase/brookite TiO_2 with oxygen vacancies. They achieved a high gaseous photocatalytic performance for acetaldehyde degradation to CO_2, which was almost twice as high as the untreated TiO_2 and 50% higher than nitrogen-doped TiO_2 under visible light. Yu *et al*. [174] also observed that solution plasma structurally modified the surface of pre-synthesized yellow TiO_2 with numerous oxygen vacancies. Upon elevated temperature treatment, the modified TiO_2 exhibited a conversion rate increased by a factor of 300 for CO_2 reduction under solar light irradiation and an increased removal rate (by a factor of 7.5) of acetaldehyde under UV light irradiation.

Defective rutile TiO_2 nanoparticles, containing oxygen vacancies and surface OH defects, were annealed up to 700 °C [175]. The average particle sizes increased from 25 and 50 nm and the optical band gaps decreased from 2.9 to 2.0 eV, changing the color from blue-gray to light-gray. The highest degradation efficiency of methylene blue was observed at an intermediate annealing temperature of 500 °C. The samples contained the lowest concentration of non-lattice oxygen atoms. The concentration and position of the defects significantly affected the mechanism of the photoactivity. In contrast to bulk defects that produce charge carrier traps acting as recombination centers, surface defects have a dual effect on the photocatalytic enhancement: they produce charge carrier traps, which reduce exciton recombination, and provide adsorption sites for oxygen and organic species.

Jedsukontorn *et al*. [36] produced defective black TiO_2 and achieved the highest photocatalytic activity for glycerol conversion (58.49% at 24 h) and values around 40 and 26% for glycolaldehyde and formaldehyde. They suggest that discharges, in addition to creating extra surface adsorption sites, also promote high ratios of Ti^{3+}/Ti^{4+} and low band gap values, which can create a mid-gap state level with an energy lower than the minimum conduction band. The presence of these mid-gap state levels prolongs the lifetime of electron-hole pairs, resulting in an amelioration of the photocatalytic performance. For longer treatment times, black TiO_2 nanoparticles agglomerate, which can also extend the lifetime of electron-hole pairs due to the interparticle charge transport.

Yu *et al*. [176] treated commercially available nitrogen-doped TiO_2 with solution plasma to modulate the surface electron traps. The introduction of electron traps with a shallow energy level promotes the de-trapping of electrons at defects with a deep energy level by light or thermal assistance, enhancing the utilization of electrons for reduction reactions like photocatalytic degradation of acetaldehyde.

Biazar *et al*. [177] associated carbon dots as cocatalyst with TiO_2 nanoparticles, both synthesized by solution plasma. The association of TiO_2 with carbon dots contributes to shifting the absorption edge at longer wavelengths and increasing the optical absorption in the visible range. The estimated direct band gap is 2.41 eV.

Pt@CoOx@N-C catalysts were synthesized by Liu *et al.* [46] by grafting Pt nanoparticles, prepared by solution plasma, onto CoO_x@nitrogen-doped porous carbon. This catalyst was designed to be used as an anode material in direct methanol fuel cells and exhibited high methanol oxidation reaction performance with a remarkable mass activity of 2400 mA $mgPt^{-1}$) as well as durability and stability (70% remained after 300 cycles).

Results are compiled in **Table 4**.

Although the mechanism of creating defects by discharges is now well identified, the specific process by which vacancies are created, their depth and accessibility by molecules to be reduced, still requires further investigations in order to better understand and optimize photoactive nanomaterials.

Photocatalysts	Chemical process	Methods	Improvement	Comments	Ref.
			ORR and HER		
$BiVO_4$	ORR in water	Surface activation	ORR rate x 1.5	Facet-dependent photoactivity	[27]
C-encapsulated WC	ORR in 0.5 M H_2SO_4 saturated in O_2	Composite catalyst	Decrease of ORR peaks from 150 to 180 kHz	High conductivity of nanocomposites	[34, 167]
Pt NP / Ketjen Black	ORR and HER in 0.5 M H_2SO_4 saturated in N_2 and O_2	improvement of NP adhesion on C support	bifunctional catalytic activity toward HER and ORR solution.	Improvement of yield and stability	[47]
Si NP / N-doped carbons	ORR in 0.1 M KOH solution saturated in N_2 and O_2	Composite catalyst	ORR activity still inferior to Pt/C	co-existence of two and four-electron pathways in ORR	[56]
PtPd / MXene nanosheets	ORR and HER in 0.1 M H_2SO_4 saturated in N_2 and O_2	Composite catalyst	Lower voltage for yielding 10 mA cm^{-2} for both HER and OER	$Ti_3C_2T_x$ nanosheets inhibit aggregation of different metal NPs	[166]
MoS_2	ORR and HER in 0.5 M H_2SO_4	Surface activation	low overpotential at 10 mA cm^{-2} current density	large surface area, low impedance, high capacitance, and fast electron transfer	[168]
			DEGRADATION OF CHEMICALS		
Pt / CoO_x@nitrogen-doped porous carbon	methanol oxidation reaction	Composite catalyst	activity superior to Pt/C (460 mA/mg_{Pt})	MOF used as precursors	[46]
WO_3	photodestruction of the rhodamine B	High specific area	Complete degradation under UV	Narrow forbidden band and large surface to volume ratio due to small size	[71]
Ag/Ga_2O_3	Photocatalytic reduction of CO_2	Composite catalyst	Higher CO production rate after UV irradiation	Reduction of performance with time by NP aggregation	[81]
WO_3	Photooxidation of bisphenol A	Surface activation	6 and 12 x higher rates than $(SO_4^-)_2$ oxidation and photodegradation	Electron and hole extraction improved by oxygen vacancies and hydrated bridging hydroxyls	[161]
			TiO_2		
Defective black TiO_2	Glycerol conversion	Surface activation	highest photocatalytic activity compared to other chemicals	high degree of defective structures (Ti^{3+}/Ti^{4+} ratio) which can shorten the band gap energy	[36]
Anatase/brookite TiO_2	Degradation of acetaldehyde	Surface activation	~twice more efficient than untreated TiO_2	more effective charge separation at anatase/brookite heterocrystalline phases	[61]
Defective rutile TiO_2	Degradation of methylene blue	Surface activation	Optimum degradation rate after annealing @500°C	Optical band gap decreases from 2.9 to 2.0 eV	[175]
Nitrogen-doped TiO_2	Degradation of acetaldehyde	Surface activation	Rate increased by 3.2 times	Introduction of electron traps with shallow energy level into N-TiO_2	[176]

Table 4 Compilation of results obtained in photocatalysis.

Biological applications

Saebnoori *et al*. [96] synthesized CuO nanoparticles ranging from 25 to 160 nm in diameter. The antibacterial results revealed that CuO samples are effective in reducing the activity of gram-negative Pseudomonas Aeruginosa and gram-positive Staphylococcus Aureus. Weerasinghe *et al*. [178] examined the antibacterial

activity of silver nanoparticles (ranging from 5.4 to 17.8 nm) against both gram-negative Escherichia Coli and gram-positive Staphylococcus Aureus. They observed inhibition of growth of colonies deposited on agar plates for both types of bacteria. Elwaki *et al*. [179] produced spherical CuO nanoparticles by discharges in water and compared their antibacterial activity with nanowires produced in the same reactor by simply replacing liquid water with argon gas. They found that both types of nanoobjects showed potent antibacterial activity against different multi-drug-resistant Acinetobacter baumannii strains, with nanowires showing superior antibacterial activity over particles. MubarakAli [114] synthesized low-molecular-weight chitosan through the depolymerization of high-molecular-weight chitosan with the solution plasma process. These aggregates showed antimicrobial activity against Escherichia Coli, Staphylococcus Aureus, and Candida Albicans with a minimal inhibitory concentration of 80–1200 $\mu g \cdot mL^{-1}$. Mohammadi *et al*. [180] prepared chitosan-coated Bi_2O_3–$Bi(OH)_3$ nanoparticles using solution plasma. The cytotoxicity of these hybrid nanoparticles on the HDF-1 cell line displayed no considerable toxicity, indicating the potential usefulness of MubarakAli's approach.

Ko *et al*. [181] developed biocomposites of hydroxypropyl methylcellulose (HPMC) and silver nanoparticles. The bactericidal activity was evaluated by measuring the sizes of inhibition zones of bacterial growth formed by the biocomposites (**Fig. 15**), which ranged from 8 to 14.3 mm. The minimal inhibition concentrations were found in the range of 10–15 $\mu g \cdot mL^{-1}$ for gram-negative bacteria (E. Coli, P. Aeruginosa, V. Vulnificus) and 25–30 $\mu g \cdot mL^{-1}$ for gram-positive bacteria (B. Cereus, S. Aureus and C. Albicans). A similar solution of alginate/Ag composites was also tested, which showed a suppression yield of 99.8% against E. Coli [53].

a

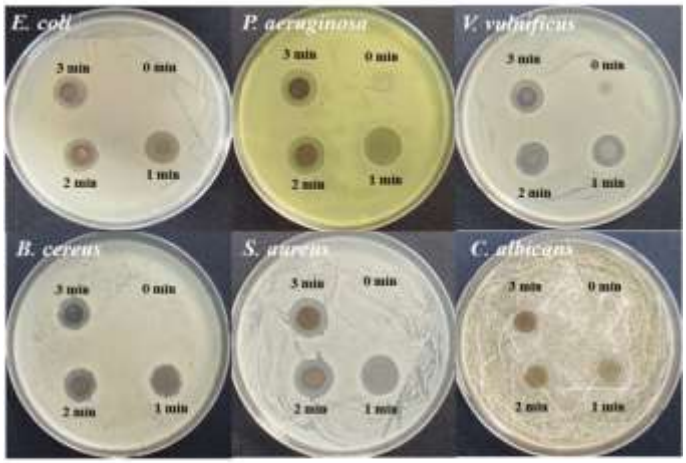

b

Pathogens	5.0% HPMC/AgNPs (mm)		
	1 min	2 min	3 min
E. coli	12.9 ± 0.06	13.3 ± 0.31	13.3 ± 0.36
P. aeruginosa	14.1 ± 0.91	14.8 ± 0.35	15.3 ± 0.78
V. vulnificus	13.8 ± 0.31	14.2 ± 0.15	14.4 ± 0.10
B. cereus	12.8 ± 0.66	12.9 ± 0.15	13.5 ± 0.20
S. aureus	14.3 ± 0.06	14.4 ± 0.10	14.5 ± 0.15
C. albicans	8.0	8.0	8.0

Fig. 15 Agar diffusion assay of the HPMC/Ag nanoparticles biocomposites: (a) inhibition zones of growth formed around the discs of 5 % HPMC discharged for 1, 2 or 3 min (b) diameters of the growth inhibition zones formed around the biocomposites on the agar plates inoculated by various pathogens. After Ko *et al.* (2023) Carbohydrate Polym 302:120341. Reproduced with permission from Elsevier.

Arkarca *et al*. [182] utilized a combination of solution plasma and pulsed electric field (3500 V, repetition 17 kHz, and pulse width 2.58 μs) for the treatment of raw milk. The temperatures reached during microbial inactivation remained low. Maillard reactions were limited, and color changes and nutritional values were

preserved. Furthermore, unique physical and chemical values of the probiotic yoghurt drink made from the milk were also maintained. One of the most important effects of plasma application was the higher number of probiotic bacteria in samples produced by this method during storage compared to all other samples. However, the authors did not mention the possible contamination by tungsten nanoparticles produced by electrode erosion.

Vu *et al*. [75] studied the acute oral cytotoxicity of selenium nanoparticles (diameter:100 to 200 nm) prepared using the solution plasma process. With doses of Se nanoparticles lower than 6 mg kg^{-1}, no deaths or signs of toxicity were observed in mice. The mean fatal dose of Se nanoparticles was determined to be 9 mg kg^{-1}, which is four times higher than that of SeO_2.

The bactericidal effects of nanoobjects are well-known, and they have been exploited in the experiments reported here based on discharges in liquids. However, the benefits of the selected processes rely more on the advantages offered by the synthesis method than on the improvement of the intrinsic properties of the selected materials. Promoting the development of new nanomaterials could be an interesting way to take advantage of discharges in liquid in this field.

CONCLUDING REMARKS

Discharges in liquids have proven to be highly effective in producing nanoobjects with controlled characteristics. They offer a low-cost, high-yield, and safe one-pot synthesis method. As demonstrated in this review, the process parameters can be adjusted to achieve the desired final properties for specific applications.

Despite their remarkable capabilities, the non-equilibrium conditions prevailing in discharges have not been fully exploited, and preliminary studies have only recently begun to investigate the alloying of multiple immiscible elements. Further research is necessary to deepen our understanding of the growth mechanisms of nanoobjects, particularly when they are non-spherical.

Additionally, the investigation of discharge parameters and their time-resolved evolution is a difficult but necessary task that can provide critical information on active species and reaction pathways. Interface processes between media also require significant research efforts, but their complexity makes it challenging to probe them. However, mastering polymerization processes, for instance, depends on understanding these processes.

Processes based on discharges in liquids have now undergone more than a decade of research, and we can anticipate significant breakthroughs in a period when the energy transition demands new and efficient nanomaterials to meet the challenges we face.

Acknowledgment
The authors acknowledge the French PIA (programme d'investissements d'avenir) project Lorraine Université d'Excellence (Ref. ANR-15-IDEX-04-LUE) for financial support.

Declarations

Ethical Approval
Not applicable

Competing interests
Not applicable

Author's Contribution
T.B participated in the bibliography research and wrote the manuscript.
A.V.N., C.N., T.G., A. N., V.M., M.B. and M.A. participated in the bibliography research and reviewed the manuscript.

Funding
A.V. Nominé's Ph.D was funded by the French PIA (programme d'investissements d'avenir) project Lorraine Université d'Excellence.

Availability of data and materials
A reasonable request to the corresponding authors may permit the data used to support the results of this study.

REFERENCES

[1] Chen Q, Li J, Li, Y (2015) A review of plasma–liquid interactions for nanomaterial synthesis. J Phys D: Appl Phys 48:424005. https://doi.org/10.1088/0022-3727/48/42/424005

[2] Saito G, Akiyama T (2016) Nanomaterial synthesis using plasma generation in liquid. J Nanomater 2015: 123696. https://doi.org/10.1155/2015/123696

[3] Saito N, Bratescu MA, Hashimi K (2017) Solution plasma: A new reaction field for nanomaterials synthesis. Jap J Appl Phys 57:0102A4. https://doi.org/10.7567/JJAP.57.0102A4

[4] Horikoshi S, Serpone N (2017) In-liquid plasma: A novel tool in the fabrication of nanomaterials and in the treatment of wastewaters. RSC adv 7:47196–47218. https://doi.org/10.1039/C7RA09600C

[5] Levchenko I, Bazaka K, Baranov O et al (2018) Lightning under water: Diverse reactive environments and evidence of synergistic effects for material treatment and activation. Appl Phys Rev 5:021103. https://doi.org/10.1063/1.5024865

[6] Yonezawa T, Čempel D, Nguyen MT (2018) Microwave-induced plasma-in-liquid process for nanoparticle production. Bull Chem Soc Jap 91:1781–1798. https://doi.org/10.1246/bcsj.20180285

[7] Prasad S, Kumar V, Kirubanandam S et al (2018) Engineered nanomaterials: Nanofabrication and surface functionalization. Chap. 11:305–340. In: Barhoum A, Makhlouf ASH (ed) Emerging applications of nanoparticles and architecture nanostructures, Elsevier, Netherlands. https://doi.org/10.1016/B978-0-323-51254-1.00011-7

[8] Rezaei F, Vanraes P, Nikiforov A at al (2019) Applications of plasma-liquid systems: A review. Materials 12:2751. https://doi.org/10.3390/ma12172751

[9] Kim HM, Saito N, Kim DW (2019) Solution plasma-assisted green synthesis of MnO_2 adsorbent and removal of cationic pollutant. J Chem 2019:1−7. https://doi.org/10.1155/2019/7494292

[10] Stancampiano A, Gallingani T, Gherardi M et al (2019) Plasma and aerosols: Challenges, opportunities and perspectives. Appl Sci 9:3861. https://doi.org/10.3390/app9183861

[11] Vandenabeele CR, Lucas S (2020) Technological challenges and progress in nanomaterials plasma surface modification–a review. Mater Sci Eng R Rep 139:100521. https://doi.org/10.1016/j.mser.2019.100521

[12] Nominé AV, Gries T, Noel C et al (2021) Synthesis of nanomaterials by electrode erosion using discharges in liquids. J Appl. Phys. 130:151101. https://doi.org/10.1063/5.0040587

[13] Sergievskaya A, Chauvin A, Konstantinidis S (2022) Sputtering onto liquids: a critical review. Beilstein J Nanotechnol 13:10–53. https://doi.org/10.3762/bjnano.13.2

[14] Chokradjaroen C, Wang X, Niu J et al (2022) Fundamentals of solution plasma for advanced materials synthesis. Mater Adv Today 14:100244. https://doi.org/10.1016/j.mtadv.2022.100244

[15] Jendrzej S, Gökce B, Epple M et al (2017) How Size Determines the Value of Gold: Economic Aspects of Wet Chemical and Laser-Based Metal Colloid Synthesis. ChemPhysChem 18:1012–1019. https://doi.org/10.1002/cphc.201601139

[16] Amans D, Cai W, Barcikowski S (2019) Status and demand of research to bring laser generation of nanoparticles in liquids to maturity. Appl Surf Sci 488:445–454. https://doi.org/10.1016/j.apsusc.2019.05.117

[17] Nakibli Y, Mazal Y, Dubi Y et al (2018) Size matters: Cocatalyst size effect on charge transfer and photocatalytic activity. Nano Lett. 18: 357-364. https://doi.org/10.1021/acs.nanolett.7b04210

[18] Yao Y, Huang Z, Xie P et al (2018) Carbothermal shock synthesis of high-entropy-alloy nanoparticles. Science 359:1489−1494. https://doi.org/10.1126/science.aan5412

[19] Chen PC, Liu X, Hedrick JL et al (2016) Polyelemental nanoparticle libraries. Science 352:1565-1569. https://doi.org/10.1126/science.aaf8402

[20] Lee S, Saito N (2018) Enhancement of nitrogen self-doped nanocarbons electrocatalyst via tune-up solution plasma synthesis. RSC Adv 8:35503−35511. https://doi.org/10.1039/c8ra06614k

[21] Liew BYY, Ranjit MS, Julaihi MRM et al (2020) Synthesis and Size Control of Aluminum Nanoparticles using Solution Plasma Process. In IOP Conference Series: Materials Science and Engineering 943:012006. https://doi.org/10.1088/1757-899X/943/1/012006

[22] Shabani M, Saebnoori E, Hassanzadeh-Tabrizi A et al (2020) Polyethylene Glycol Coated $NiFe_2O_4$ Nanoparticles Produced by Solution Plasma Method for Biomedical Applications. J Adv Mater Process 8:55−60.

[23] Martin J, Haraux P, Ntomprougkidis V et al (2020) Characterization of metal oxide micro/nanoparticles elaborated by plasma electrolytic oxidation of aluminium and zirconium alloys. Surf Coat Technol 397:125987. https://doi.org/10.1016/j.surfcoat.2020.125987

[24] Takai O (2008) Solution plasma processing (SPP). Pure Appl Chem 80:2003–2011. https://doi.org/10.1351/pac200880092003

[25] Saito N, Hieda J, Takai O (2009) Synthesis process of gold nanoparticles in solution plasma. Thin Solid Film 518:912–917. https://doi.org/10.1016/j.tsf.2009.07.156

[26] Chantaramethakul J, Choophun N, Chokradjaroen C et al (2023) Morphological Evolution of Gold Nanoparticles Synthesized via Solution Plasma Sputtering: Effect of Sodium Chloride Concentration and Storage Time. J Phys Chem C 127:3184−3193. https://doi.org/10.1021/acs.jpcc.2c06474

[27] Che G, Wang D, Wang C et al (2020) Solution plasma boosts facet-dependent photoactivity of decahedral $BiVO_4$. Chem Eng J 397:125381. https://doi.org/10.1016/j.cej.2020.125381

[28] Chen Z, Wang J, Onyshchenko I et al (2021) Efficient and Green Synthesis of SiOC Nanoparticles at Near-Ambient Conditions by Liquid-Phase Plasma. ACS Sustainable Chem Eng 9:7728−7736. https://doi.org/10.1021/acssuschemeng.0c08637

[29] Chokradjaroen C, Kato S, Fujiwara K et al (2020) A comparative study of undoped boron-doped and boron/fluorine dual-doped carbon nanoparticles obtained via solution plasma as catalysts for the oxygen reduction reaction. Sustain Energy Fuels 4:4570−4580. https://doi.org/10.1039/D0SE00708K

[30] Chokradjaroen C, Watanabe H, Ishii T et al (2021) Simultaneous synthesis of graphite-like and amorphous carbon materials via solution plasma and their evaluation as additive materials for cathode in Li–O_2 battery. Sci Rep 11:6261. https://doi.org/10.1038/s41598-021-85392-2

[31] Hu X, Shen X, Takai O et al (2013) Facile fabrication of PtAu alloy clusters using solution plasma sputtering and their electrocatalytic. J Alloys Compounds 552:351–355. https://doi.org/10.1016/j.jallcom.2012.08.033

[32] Huang Y, Wang C, Wang R et al (2023) Ethanol Solution Plasma Loads Carbon Dots onto 2D HNb_3O_8 for Enhanced Photocatalysis. ACS Appl Mater Interf 15:1157−1166. https://doi.org/10.1021/acsami.2c18551

[33] Islam MZ, Watthanaphanit A, Chae S et al (2021) Li–air battery and ORR activity of nanocarbons produced with good synthesis rate by solution plasma process. Mater Adv 2:2636−2641. https://doi.org/10.1039/d0ma00926a

[34] Islam Z, Watthanaphanit A, Chae S et al (2021) Structure and properties of nanocarbons-encapsulated WC synthesized by solution plasma process in palm oils. Mater Express 11:1602−1607. https://doi.org/10.1166/mex.2021.2034

[35] Jang HJ, Shin BJ, Jung EY et al (2023) Polypyrrole film synthesis via solution plasma polymerization of liquid pyrrole. Appl Surf Sci 608:155129. https://doi.org/10.1016/j.apsusc.2022.155129

[36] Jedsukontorn T, Ueno T, Saito N et al (2018). Narrowing band gap energy of defective black TiO_2 fabricated by solution plasma process and its photocatalytic activity on glycerol transformation. J Alloys Compd 757:188−199. https://doi.org/10.1016/j.jallcom.2018.05.046

[37] Jung EY, Park CS, Shin JG et al (2022) Characteristics of polyaniline nanoparticles prepared by electrochemical solution plasma process for flexible devices. Mol Cryst Liq Cryst 733:114−124. https://doi.org/10.1080/15421406.2021.1972206

[38] Kim DY, Li OL, Kang J (2020) Novel synthesis of highly phosphorus-doped carbon as an ultrahigh-rate anode for sodium ion batteries. Carbon 168:448−457. https://doi.org/10.1016/j.carbon.2020.07.021

[39] Kim K, Chokradjaroen C, Saito N (2020) Solution plasma: New synthesis method of N-doped carbon dots as ultra-sensitive fluorescence detector for 2 4 6-trinitrophenol. Nano Express 1:020043. https://doi.org/10.1088/2632-959X/abb9fa

[40] Kim K, Chae S, Choi PG et al (2021) Facile synthesis of ZnO nanobullets by solution plasma without chemical additives. RSC Adv 11:26785−26790. https://doi.org/10.1039/d1ra05008g

[41] Kim K, Chae S, Masuda Y et al (2022) Morphology control of ZnO nanostructures using Zn and W electrodes in solution plasma process. Mater Lett 309:131349. https://doi.org/10.1016/j.matlet.2021.131349

[42] Kum DS, Park CS, Kim HJ et al (2018) Synthesis of carbon materials by solution plasma reactor with stable discharge and advanced plasma spray deposition method. Mol Cryst Liq Cryst 663:115−123. https://doi.org/10.1080/15421406.2018.1468645

[43] Lee SH (2018) Solution Plasma Synthesis of BNC Nanocarbon for Oxygen Reduction Reaction. J Korean Inst Surf Eng 51:332−336. https://doi.org/10.5695/JKISE.2018.51.5.332

[44] Lee H, Lee WJ, Park YK et al (2018) Liquid phase plasma synthesis of iron oxide nanoparticles on nitrogen-doped activated carbon resulting in nanocomposite for supercapacitor applications. Nanomaterials 8:190. https://doi.org/10.3390/nano8040190

[45] Li OL, Shi Z, Lee H et al (2019) Enhanced electrocatalytic stability of platinum nanoparticles supported on sulfur-doped carbon using in-situ solution plasma. Sci Rep 9:1−10. https://doi.org/10.1038/s41598-019-49194-x

[46] Liu Z, Song K, Yang B et al (2021) Solution plasma method assisted with MOF for the synthesis of Pt@ CoOx@ NC composite catalysts with enhanced methanol oxidation performance. Int J Hydrog Energy 46:39743−39753. https://doi.org/10.1016/j.ijhydene.2021.09.194

[47] Mani-Lata C, Hussakan C, Panomsuwan G (2020) Fast and Facile Synthesis of Pt Nanoparticles Supported on Ketjen Black by Solution Plasma Sputtering as Bifunctional HER/ORR Catalysts. J Compos Sci 4:121. https://doi.org/10.3390/jcs4030121

[48] Minami E, Miyamoto T, Kawamoto H (2022) Decomposition of Saccharides and Alcohols in Solution Plasma for Hydrogen Production. Hydrogen 3:333−347. https://doi.org/10.3390/hydrogen3030020

[49] Morishita T, Ueno T, Panomsuwan G et al (2016) Fastest formation routes of nanocarbons in solution plasma processes. Sci Rep 6:1–13. https://doi.org/10.1038/srep36880

[50] MubarakAli D, Park BR, Rhee WJ et al (2018) Antioxidant potentials of nanoceria synthesized by solution plasma process and its biocompatibility study. Arch biochem biophys 645:42−49. https://doi.org/10.1016/j.abb.2018.02.003

[51] MubarakAli D, Lee M, Manzoor MA et al (2021) Production of Oligoalginate via Solution Plasma Process and Its Capability of Biological Growth Enhancement. Appl Biochem Biotechnol 193:4097−4112. https://doi.org/10.1007/s12010-021-03640-7

[52] Mukasa S, Masuda T, Kimura E et al (2018) Synthesis of Tin Nanoparticles by Pulse Discharge in Water and Aqueous Gelatin Solution. J Japan Instit Energy 97:186−190. https://doi.org/10.3775/jie.97.186

[53] Nam S, MubarakAli D, Kim J (2016) J Characterization of Alginate/Silver Nanobiocomposites Synthesized by Solution Plasma Process and Their Antimicrobial Properties, J Nanomater 2016:4712813. https://doi.org/10.1155/2016/4712813

[54] Oruncak B, Özkan M, Akyüz A (2020) Gold nanoparticle synthesis by electrohydrodynamic discharge. Arab J Geosci 13:1−5. https://doi.org/10.1007/s12517-020-05688-x

[55] Özkan M, Oruncak B, Çevik S (2020) Aqueous Solution of $VOSO_4 \cdot xH_2O$ in Solution Plasma Process. El-Cezerî J Sci Eng 7:543−548. https://doi.org/10.31202/ecjse.666094

[56] Panomsuwan G, Chantaramethakul J, Chokradjaroen C et al (2019) In situ solution plasma synthesis of silver nanoparticles supported on nitrogen-doped carbons with enhanced oxygen reduction activity. Mater Lett 251:135–139. https://doi.org/10.1016/j.matlet.2019.05.052

[57] Park CS, Kum DS, Kim JC et al (2018) Simple one-step synthesis of carbon nanoparticles from aliphatic alcohols and n-hexane by stable solution plasma process. Carbon Lett 28:31−37. https://doi.org/10.5714/CL.2018.28.031

[58] Phan PQ, Chae S, Pornaroontham P et al (2020) In situ synthesis of copper nanoparticles encapsulated by nitrogen-doped graphene at room temperature via solution plasma. RSC Adv 10:36627−36635. https://doi.org/10.1039/d0ra07162e

[59] Phan PQ, Naraprawatphong R, Pornaroontham P et al (2021) N-Doped few-layer graphene encapsulated Pt-based bimetallic nanoparticles via solution plasma as an efficient oxygen catalyst for the oxygen reduction reaction. Mater Adv 2:322−335. https://doi.org/10.1039/d0ma00718h

[60] Pimklang T, Watthanaphanit A, Pakawatpanurut P (2022)Novel green synthesis of graphene oxide-manganese dioxide using solution plasma process for energy storage, Chem Eng J 442:136244. https://doi.org/10.1016/j.cej.2022.136244

[61] Pitchaimuthu S, Honda K, Suzuki S et al (2018) Solution plasma process-derived defect-induced heterophase anatase/brookite TiO_2 nanocrystals for enhanced gaseous photocatalytic performance. ACS Omega 3:898−905. https://doi.org/10.1021/acsomega.7b01698

[62] Pornaroontham P, Panomsuwan G, Chae S et al (2019) Nitriding an oxygen-doped nanocarbonaceous sorbent synthesized via solution plasma process for improving CO_2 adsorption capacity. Nanomater 9:1776. https://doi.org/10.3390/nano9121776

[63] Prasertsung I, Kaewcharoen S, Kunpinit K et al (2019) Enhanced degradation of methylene blue by a solution plasma process catalyzed by incidentally co-generated copper nanoparticles. Water Sci Technol 79:967−974. https://doi.org/10.2166/wst.2019.035

[64] Qin L, Lee S, Ha J et al (2023) Selective production of value-added chemicals from cellulosic biomass waste via plasma-synthesized catalysts. Catal Today 114030 (available online). https://doi.org/10.1016/j.cattod.2023.02.007

[65] Romero Valenzuela AE, Chokradjaroen C, Thiangtham S et al (2022) Hierarchical Porous Carbon Fibers Synthesized by Solution-Plasma-Generated Soot Deposition and Their CO_2 Adsorption Capacity. Coatings 12:1620. https://doi.org/10.3390/ma16030906

[66] Saqib ANS, Huong NTT, Kim SW (2021) Structural and magnetic properties of highly Fe-doped ZnO nanoparticles synthesized by one-step solution plasma process. J Alloys Compd 853:157153. https://doi.org/10.1016/j.jallcom.2020.157153

[67] Saymung R, Watthanaphanit A, Saito N et al (2022) Solution plasma process for synthesizing polydiacetylene materials: Toward industrial utilization of colorimetric sensors. J Indus Eng Chem 106:243–252. https://doi.org/10.1016/j.jiec.2021.10.035

[68] Shin JG, Park CS, Jung EY et al (2019) Synthesis of a polyaniline nanoparticle using a solution plasma process with an Ar gas bubble channel. Polymers 11:105. https://doi.org/10.3390/polym11010105

[69] Shin JG, Park CS, Kim HJ, et al (2019) Preparation and synthesis of carbon nanomaterials from 1-hexanol by solution plasma process with Ar/O_2 gas bubbles. Mol Cryst Liq Cryst 678:20–32. https://doi.org/10.1080/15421406.2019.1597524

[70] Shin JG, Shin BJ, Jung EY et al (2020) Effects of a dielectric barrier discharge (DBD) on characteristics of polyaniline nanoparticles synthesized by a solution plasma process with an Ar gas bubble channel. Polymers 12:1939. https://doi.org/10.3390/polym12091939

[71] Sirotkin NA, Khlyustova AV, Titov VA. et al (2020) Synthesis and Photocatalytic Activity of WO_3 Nanoparticles Prepared by Underwater Impulse Discharge. Plasma Chem Plasma Process 40:571–587. https://doi.org/10.1007/s11090-019-10048-z

[72] Tipplook M, Pornaroontham P, Watthanaphanit A et al (2019) Liquid-phase plasma-assisted in situ synthesis of amino-rich nanocarbon for transition metal ion adsorption. ACS App Nano Mater 3:218−228. https://dx.doi.org/10.1021/acsanm.9b01915

[73] Treepet S, Chokradjaroen C, Kim K et al (2022) Saccharide-originated fluorescent carbon dots synthesized by in-liquid plasma with controlled orderliness of carbon core through precursor alteration for selective and rapid metal ion detection Materials Today Chemistry 26:101139. https://doi.org/10.1016/j.mtchem.2022.101139

[74] Van Hao N, Van Dang N, Van Tu N et al (2020) Facile synthesis of graphene oxide from graphite rods of recycled batteries by solution plasma exfoliation for removing Pb from water. RSC Adv 10:41237–41247. https://doi.org/10.1039/d0ra07723b

[75] Vu TT, Nguyen DT, Nguyen TH et al (2022) One-Step Solution Plasma-Mediated Preparation of Se Nanoplarticles and Evaluating Their Acute Oral Toxicity in Mice. Sustainability 14:10294. https://doi.org/10.3390/su141610294

[76] Xing Y, Wang C, Li D et al (2022) Solution Plasma Processing Single-Atom Au_1 on CeO_2 Nanosheet for Low Temperature Photo-Enhanced Mars–van Krevelen CO Oxidation. Adv Funct Mater 32:2207694. https://doi.org/10.1002/adfm.202207694

[77] Yan X, Duan P, Zhang F et al (2019) Stable single-atom platinum catalyst trapped in carbon onion graphitic shells for improved chemoselective hydrogenation of nitroarenes. Carbon 143:378–384. https://doi.org/10.1016/j.carbon.2018.11.021

[78] Yang B, Qiao J, Yu Y et al (2020) The simple-preparation of Cu–Ni/CuO–NiO using solution plasma for application in a glucose enzyme-free sensor. New J Chem 44:10806–10812. https://doi.org/10.1039/D0NJ01464H

[79] Yang B, Yu Y, Qiao J et al (2020) Solution plasma method direct synthesis of Au/CuO nanoparticles for glucose enzyme-free detection. J Mater Sci: Mater Electron 31:12983-12990. https://doi.org/10.1007/s10854-020-03851-4

[80] Yang B, Yu Y, Qiao J et al (2020) Solution plasma method for the preparation of Cu-Ni/CuO-NiO with excellent methanol electrocatalytic oxidation performance. Appl Surf Sci 513:145808. https://doi.org/10.1016/j.apsusc.2020.145808

[81] Yoshida T, Yamamoto N, Mizutani T et al (2018) Synthesis of Ag nanoparticles prepared by a solution plasma method and application as a cocatalyst for photocatalytic reduction of carbon dioxide with water. Catal Today 303:320–326. https://doi.org/10.1016/j.cattod.2017.08.047

[82] Zhou J, An X, Tang Q et al (2020) Dual channel construction of WO_3 photocatalysts by solution plasma for the persulfate-enhanced photodegradation of bisphenol A. Appl Catal B: Environ 277:119221. https://doi.org/10.1016/j.apcatb.2020.119221

[83] Ziashahabi A, Poursalehi R, Naseri N (2018) Shed light on submerged DC arc discharge synthesis of low band gap gray Zn/ZnO nanoparticles: Formation and gradual oxidation mechanism. Adv Powder Technology 29:1246–1254. https://doi.org/10.1016/j.apt.2018.02.017

[84] Li CJ, Cao X, Li WH et al (2019) Co-synthesis of CuO-ZnO nanoflowers by low voltage liquid plasma discharge with brass electrode. J Alloys Compd 773:762−769. https://doi.org/10.1016/j.jallcom.2018.09.250

[85] Hamdan A, Noël C, Belmonte T (2014) Synthesis of carbon fibres by electrical discharges in heptane. Mater Lett 135:115–118. https://doi.org/10.1016/j.matlet.2014.07.158

[86] Al Anbouri MHS, Yii BWM, Yek PNY et al (2018) Effect of electrolyte concentration during solution plasma on copper nanoparticle size. In IOP Conf Series: Mater Sci Eng 429:012084. https://doi.org/10.1088/1757-899X/429/1/012084

[87] Gromov A, Nalivaiko A, Fehn T et al (2019) Cathode plasma electrolysis in diluted potassium hydroxide solutions: Particles formation and energetic estimation. J. Electroanal Chem 844:155–160. https://doi.org/10.1016/j.jelechem.2019.04.065

[88] Lim DCZS, Julaihi MRM (2019) Fabrication of solar cell using titanium, zinc, carbon and gold nanoparticles. IOP Conf. Ser.: Mater. Sci. Eng. 625:012017. https://doi.org/10.1088/1757-899X/625/1/012017

[89] Rocher S, Botrel R, Durut F et al (2018) Ultra-low density metallic foams synthesized by contact glow discharge electrolysis (CGDE) for laser experiments. Eur Phys J Appl Phys 81:10803. https://doi.org/10.1051/epjap/2017170206

[90] Samimi-Sedeh S, Saebnoori E, Talaiekhozani A et al (2019) Assessing the efficiency of sodium ferrate production by solution plasma process. Plasma Chem Plasma Process 39:769−786. https://doi.org/10.1007/s11090-019-09989-2

[91] Wang B, Yu J, Lu Q et al (2022) Preparation of Mn_3O_4 microspheres via glow discharge electrolysis plasma as a high-capacitance supercapacitor electrode material. J Alloys Compounds 926:166775. https://doi.org/10.1016/j.jallcom.2022.166775

[92] Yu J, Wang B, Lu Q et al (2022). Fabrication of Fe_3O_4 nanoparticles by using cathode glow discharge electrolysis plasma and its electrochemical properties. Electrochim Acta 427:140843. https://doi.org/10.1016/j.electacta.2022.140843

[93] Yu J, Wang B, Lu Q et al. (2023) Cathode glow discharge electrolysis synthesis of flower-like β-Ni(OH)2 microsphere for high-performance supercapacitor. Chem Eng J 453:139769. https://doi.org/10.1016/j.cej.2022.139769

[94] Xiu M, Cao X, Lu Y et al (2023) Electric-field oriented self-assembly of Mn_3O_4 nanostructures driven by liquid plasma discharge for super capacitor. Electrochim Acta 439:141620. https://doi.org/10.1016/j.electacta.2022.141620

[95] Saito G, Nakasugi Y, Yamashita T et al (2014) Solution plasma synthesis of bimetallic nanoparticles. Nanotechnol 25:135603. https://doi.org/10.1088/0957-4484/25/13/135603

[96] Saebnoori E, Koupaei N, Hassanzadeh Tabrizi S A (2022) The solution plasma synthesis, characterisation, and antibacterial activities of dispersed CuO nanoparticles. Mater Technol 37:1220-1229. https://doi.org/10.1080/10667857.2021.1929719

[97] Belmonte T, Hamdan A, Kosior F et al (2014) Interaction of discharges with electrode surfaces in dielectric liquids: application to nanoparticle synthesis, J Phys D: Appl Phys 47(22):224016. https://doi.org/10.1088/0022-3727/47/22/224016

[98] Kim BH, Kim, SJ, Chung M et al (2013) Bipolar pulsed electrical discharge for decomposition of methylene blue in aqueous TiO_2 nanoparticle dispersions. J Nanosci Nanotechnol 13(3):1966−1969. https://doi.org/10.1166/jnn.2013.6972

[99] Hamdan A, Černevičs K, Cha MS (2017). The effect of electrical conductivity on nanosecond discharges in distilled water and in methanol with argon bubbles. J Phys D: Appl Phys 50(18):185207. https://doi.org/10.1088/1361-6463/aa6969

[100] Lee H, Park SH, Kim SJ et al (2014) Synthesis of tin and tin oxide nanoparticles using liquid phase plasma in an aqueous solution. Microelectron Engin 126:153–157. https://doi.org/10.1016/j.mee.2014.07.014

[101] Lee H, Park SH, Jung SC et al (2013) Preparation of nonaggregated silver nanoparticles by the liquid phase plasma reduction method. J Mater Res 28:1105–1110. https://doi.org/10.1557/jmr.2013.59

[102] Hamdan A, Noël C, Ghanbaja J et al (2013) Synthesis of platinum embedded in amorphous carbon by micro-gap discharge in heptane. Mater Chem Phys 142:199–206. https://doi.org/10.1016/j.matchemphys.2013.07.006

[103] Hamdan A, Noel C, Kosior F et al (2013) Impacts created on various materials by micro-discharges in heptane: Influence of the dissipated charge. J Appl Phys 113(4):043301. https://doi.org/10.1063/1.4780786

[104] Lee H, Chung M, Ahn H-G et al (2015) Effect of the Surfactant on Size of Nickel Nanoparticles Generated by Liquid-Phase Plasma Method. Int J Precis Eng Manuf 16:1305-1310. https://doi.org/10.1007/s12541-015-0170-6

[105] Saito G, Hosokai S, Tsubota M et al (2011) Synthesis of copper/copper oxide nanoparticles by solution plasma. J Appl Phys 110:023302. https://doi.org/10.1063/1.3610496

[106] Bratescu MA, Cho SP, Takai O et al (2011). Size-controlled gold nanoparticles synthesized in solution plasma. J Phys Chem C 115(50):24569–24576. https://doi.org/10.1021/jp207447c

[107] Vanecht E, Binnemans K, Seo JW et al (2011) Growth of sputter-deposited gold nanoparticles in ionic liquids. Phys Chem Chem Phys 13:13565−13571. https://doi.org/10.1039/C1CP20552H

[108] Titov V, Nikitin D, Naumova I et al (2020) Dual-mode solution plasma processing for the production of chitosan/Ag composites with the antibacterial effect. Materials 13:4821. https://doi.org/10.3390/ma13214821

[109] Choukourov A (2019) Solution plasma processing of natural polymer-based materials. Izv. Vyssh. Uchebn. Zaved. Khim. Khim. Tekhnol. 62:4−30. https://doi.org/10.6060/ivkkt.20196207.5995

[110] Titova YV, Voronova MI, Maksimov AI (2008) Influence of gas-discharge plasma treatment in the electrolyte bulk on the cellulose properties. Russ J Appl Chem 81: 854–857. https://doi.org/10.1134/S107042720805025X

[111] Surov OV, Voronova MI, Rubleva NV et al (2018) A novel effective approach of nanocrystalline cellulose production: oxidation–hydrolysis strategy. Cellulose25:5035–5048. https://doi.org/10.1007/s10570-018-1910-4

[112] Chokradjaroen C, Rujiravanit R, Theeramunkong S et al (2018) Degradation of chitosan hydrogel dispersed in dilute carboxylic acids by solution plasma and evaluation of anticancer activity of de-graded products. Jpn J Appl Phys 57:24–26. https://doi.org/10.7567/JJAP.57.0102B5

[113] Chokradjaroen C, Theeramunkong S, Yui H et al (2018) Cytotoxicity against cancer cells of chitosan oligosaccharides prepared from chitosan powder degraded by electrical discharge plasma. Carbohydr Polym (2018) 201:20–30. https://doi.org/10.1016/j.carbpol.2018.08.037

[114] MubarakAli D, Lee SY, Kim JW (2018) Solution plasma mediated formation of low molecular weight chitosan and its application as a biomaterial. Int J Biol Macromol 118:1511–1517. https://doi.org/10.1016/j.ijbiomac.2018.06.168

[115] Prasertsung I, Damrongsakkul S, Saito N (2013) Crosslinking of a Gelatin Solutions Induced by Pulsed Electrical Discharges in Solutions. Plasma Process Polym 10: 792–797. https://doi.org/10.1002/ppap.201200148

[116] Watthanaphanit A, Saito N (2018) Solution plasma applications for the synthesis/modification of inorganic nanostructured materials and the treatment of natural polymers. Jpn J Appl Phys 57:1–10. https://doi.org/10.7567/JJAP.57.0102A3

[117] Park YS, Kodama S, Sekiguchi H (2021) Preparation of Metal Nitride Particles Using Arc Discharge in Liquid Nitrogen. Nanomaterials 11:2214. https://doi.org/10.3390/nano11092214

[118] Panteleimonov R, Korduban O, Ogenko V et al (2020) Synthesis of graphene-like structures by a plasma-arc discharge in liquid nitrogen. Ukrainian Chem J, 86(10):88–94. https://doi.org/10.33609/2708-129X.86.10.2020.88-94

[119] Hamdan A, Noël C, Ghanbaja J et al (2014) Comparison of Aluminium Nanostructures Created by Discharges in Various Dielectric Liquids. Plasma Chem Plasma Process 34:1101–1114. https://doi.org/10.1007/s11090-014-9564-y

[120] Sari AH, Khazali A, Parhizgar SS (2018) Synthesis and characterization of long-CNTs by electrical arc discharge in deionized water and NaCl solution. Int Nano Lett 8:19–23. https://doi.org/10.1007/s40089-018-0227-5

[121] Üstün T, Eskizeybek V, Toumiat O et al (2022) $CdSO_4$-CdS Composite nanowires synthesized by arc discharge method. Niğde Ömer Halisdemir Üniversitesi Mühendislik Bilimleri Dergisi, 11(3):813–818. https://doi.org/10.28948/ngmuh.820329

[122] Horiguchi G, Chikaoka Y, Shiroishi H et al (2018). Synthesis of Pt nanoparticles as catalysts of oxygen reduction with microbubble-assisted low-voltage and low-frequency solution plasma processing. J Power Sources 382: 69–76. https://doi.org/10.1016/j.jpowsour.2018.02.017

[123] Yii BWM, Yek PYN, Ranjit MS et al (2020) Study on size control of TiO_2 nanoparticles synthesized using solution plasma process. In IOP Conf Series: Mater Sci Eng 943:012009. https://doi.org/10.1088/1757-899X/943/1/012009

[124] Pootawang P (2011) Solution plasma synthesis and characteristic for mesoporous silica and metal nanoparticles system (Doctoral dissertation, Dissertation, Nagoya University, Nagoya).

[125] Lu Q, Wang X, Yu J et al (2020) Synthesis of spindle-like CuO nanoparticles by using cathode glow discharge electrolysis plasma. Mater Lett 264:127316. https://doi.org/10.1016/j.matlet.2020.127316

[126] Lu Q-F, Li J-L, Yu J et al (2021) Preparation of Ta_2O_5 nanoparticles by using cathode glow discharge electrolysis. Mater Res Express 8:125011. https://doi.org/10.1088/2053-1591/ac3e94

[127] Gudmundsson JT, Thorsteinsson EG (2007) Oxygen discharges diluted with argon: dissociation processes. Plasma Sources Sci Technol 16(2):399–412. https://doi.org/10.1088/0963-0252/16/2/025

[128] Ualkhanova MN, Zhakypov AS, Nemkayeva RR et al (2023) Synthesis of Graphite-Encapsulated Ni Micro and Nanoparticles Using Liquid-Phase Arc Discharge. Energies 16:1450. https://doi.org/10.3390/en16031450

[129] Bratescu MA, Kim K, Saito N (2019) Quantitative spectrochemical analysis of solution plasma in aromatic molecules. Plasma Process Polym 16:e1900012. https://doi.org/10.1002/ppap.201900012

[130] Chae S, Panomsuwan G, Bratescu MA et al (2019) p-Type doping of graphene with cationic nitrogen. ACS Appl Nano Mater 2:1350–1355. https://doi.org/10.1021/acsanm.8b02237

[131] Niu J, Chokradjaroen C, Saito N (2022) Graphitic N-doped graphene via solution plasma with a single dielectric barrier. Carbon 199:347−356. https://doi.org/10.1016/j.carbon.2022.08.032

[132] Yasuda HK (2005) Some important aspects of plasma polymerization. Plasma Process Polym 2(4):293–304. https://doi.org/10.1002/ppap.200400071

[133] Niu J, Chokradjaroen C, Sawada Y et al (2022) Plasma–Solution Junction for the Formation of Carbon Material. Coatings 12:1607. https://doi.org/10.3390/coatings12111607

[134] Kim HJ, Shin JG, Park CS et al (2018) In-liquid plasma process for size-and shape-controlled synthesis of silver nanoparticles by controlling gas bubbles in water. Mater 11(6):891. https://doi.org/10.3390/ma11060891

[135] Dobes K, P Naderer P, Lachaud N et al (2011) Sputtering of tungsten by N^+ and N_2^+ ions: investigations of molecular effects. Phys. Scr. T145:014017. https://doi.org/10.1088/0031-8949/2011/T145/014017. See also Somogyvári Z, Langer GA, Erdélyi G et al (2012) Sputtering yields for low-energy Ar^+- and Ne^+-ion bombardment. Vacuum 86(12):1979-1982. https://doi.org/10.1016/j.vacuum.2012.03.055. Sugiyama K, Schmid K, Jacob W (2016) Sputtering of iron, chromium and tungsten by energetic deuterium ion bombardment. Nucl Mater Energy 8:1-7. https://doi.org/10.1016/j.nme.2016.05.016

[136] Ahmadi N, Poursalehi R, Kirilyuk A et al (2019) Effect of gold plasmonic shell on nonlinear optical characteristics and structure of iron based nanoparticles. Appl Surf Sci 479:114–118. https://doi.org/10.1016/j.apsusc.2019.02.073

[137] Gupta SKS (2015) Contact glow discharge electrolysis: its origin, plasma diagnostics and non-faradaic chemical effects. Plasma Sources Sci Technol 24:063001. https://doi.org/10.1088/0963-0252/24/6/063001

[138] Takeuchi N, Kawahara K, Gamou F, et al (2020) Observation of solution plasma in water-ethanol mixed solution for reduction of graphene oxide. Int J Plasma Environ Sci Technol 14:e01009. https://doi.org/10.34343/ijpest.2020.14.e01009

[139] Belmonte T, Kabbara H, Noël C et al (2018) Analysis of Zn I emission lines observed during a spark discharge in liquid nitrogen for zinc nanosheet synthesis. Plasma Sources Sci Technol 27:074004. https://doi.org/10.1088/1361-6595/aacee2

[140] Nominé AV, Noel C, Gries T et al (2021) Study by Optical Spectroscopy of Bismuth Emission in a Nanosecond-Pulsed Discharge Created in Liquid Nitrogen. Molecules 26:7403. https://doi.org/10.3390/molecules26237403

[141] Bera D, Brinley E, Kuiry SC et al (2005) Optoelectronically automated system for carbon nanotubes synthesis via arc-discharge in solution. Rev Sci Instrum 76:033903. https://doi.org/10.1063/1.1857465

[142] Calvo F (2015) Thermodynamics of nanoalloys. Phys Chem Chem Phy 17(42):27922–27939. https://doi.org/10.1039/C5CP00274E

[143] Pootawang P, Saito N, Takai O et al (2012) Synthesis and characteristics of Ag/Pt bimetallic nanocomposites by arc-discharge solution plasma processing. Nanotechnol 23:395602. https://doi.org/10.1088/0957-4484/23/39/395602

[144] Kabbara H, Ghanbaja J, Noël C et al (2018) Nano-objects synthesized from Cu, Ag and Cu28Ag72 electrodes by submerged discharges in liquid nitrogen, Mater Chem Phys 217:371–378. https://doi.org/10.1016/j.matchemphys.2018.07.004

[145] Trad M, Nominé A, Noel C et al (2020) Evidence of alloy formation in CoNi nanoparticles synthesized by nanosecond-pulsed discharges in liquid nitrogen. Plasma Process Polym 17:e1900255. https://doi.org/10.1002/ppap.201900255

[146] Hamdan A, Cha MS (2018) Carbon-based nanomaterial synthesis using nanosecond electrical discharges in immiscible layered liquids: N-heptane and water. J Phys D: Appl Phys 51(24):244003. https://doi.org/10.1088/1361-6463/aac46f

[147] Hamdan A, Stafford L (2022) A Versatile Route for Synthesis of Metal Nanoalloys by Discharges at the Interface of Two Immiscible Liquids. Nanomaterials 12:3603. https://doi.org/10.3390/nano12203603

[148] Saito N, Ueno T, Bratescu MA et al (2019) Synthesis of Nanomaterials Using Solution Plasma Process. Novel Structured Metallic and Inorganic Materials. Y. Setsuhara et al. (eds.), Novel Structured Metallic and Inorganic Materials. Springer Nature Singapore Pte Ltd. Chap 23. 343–355. https://doi.org/10.1007/978-981-13-7611-5

[149] Wang R, Zuo S, Wu D et al (2014) Microplasma-Assisted Synthesis of Colloidal Gold Nanoparticles and Their Use in the Detection of Cardiac Troponin I (cTn-I). Plasma Process Polym 12:380–391. https://doi.org/10.1002/ppap.201400127

[150] Saito G, Nakasugi Y, Akiyama T (2015) Generation of solution plasma over a large electrode surface area. J Appl Phys 118:023303. https://doi.org/10.1063/1.4926493

[151] Saito G, Sasaki H, Takahashi H et al (2018) Solution-plasma-mediated synthesis of Si nanoparticles for anode material of lithium-ion batteries. Nanomaterials 8:286. https://doi.org/10.3390/nano8050286

[152] Pootawang P, Saito N, Lee SY (2013) Discharge time dependence of a solution plasma process for colloidal copper nanoparticle synthesis and particle characteristics. Nanotechnol 24:055604. https://doi.org/10.1088/0957-4484/24/5/055604

[153] Jiang, XC, Chen WM., Chen CY et al (2011) Role of temperature in the growth of silver nanoparticles through a synergetic reduction approach. Nanoscale Res Lett 6:1–9. https://doi.org/10.1007/s11671-010-9780-1

[154] Penn RL, Banfield JF (1998) Imperfect oriented attachment: dislocation generation in defect-free nanocrystals. Science 281:969–971. https://doi.org/10.1126/science.281.5379.969

[155] Petroski JM, Wang ZL, Green TC et al (1998) Kinetically controlled growth and shape formation mechanism of platinum nanoparticles. J Phys Chem B, 102:3316−3320. https://doi.org/10.1021/jp981030f

[156] Treesukkasem N, Chokradjaroen C, Theeramunkong S et al (2019) Synthesis of Au Nanoparticles in Natural Matrices by Liquid-Phase Plasma: Effects on Cytotoxic Activity against Normal and Cancer Cell Lines ACS Appl Nano Mater 2:8051−8062. https://doi.org/10.1021/acsanm.9b02106

[157] Tran MH, Jeong HK (2018) Modification of titanium dioxide by solution plasma. J Phys Chem Solids 121:292–297. https://doi.org/10.1016/j.jpcs.2018.05.047

[158] Zhu S, Yu Z, Zhang L et al (2021) Solution plasma-synthesized black TiO_2 nanoparticles for solar–thermal water evaporation. ACS Appl Nano Mater 4:3940–3948. https://doi.org/10.1021/acsanm.1c00322

[159] Yu F, Di L (2020) Plasma for Energy and Catalytic Nanomaterials. Nanomater 10:333. https://doi.org/10.3390/nano10020333

[160] Wang R, Che G, Wang C et al (2022) Alcohol plasma processed surface amorphization for photocatalysis. ACS Catal. 12:12206–12216. https://doi.org/10.1021/acscatal.2c03427

[161] Zhou Y, Nishina Y (2020) Bottom-up synthesis of nitrogen-doped nanocarbons by a combination of metal catalysis and a solution plasma process. Nanoscale Adv 2:4417–4420. https://doi.org/10.1039/d0na00327a

[162] Liu J, He L, Zhao S et al (2023) Plasma-Assisted Defect Engineering on p-n Heterojunction for High-Efficiency Electrochemical Ammonia Synthesis. Adv Sci 2205786. https://doi.org/10.1002/advs.202205786

[163] Niyitanga T, Jeong HK (2021) Modification of thermally reduced graphite oxide and molybdenum disulfide by solution plasma for hydrogen evolution reaction. Mater Chem Phys 263:124345. https://doi.org/10.1016/j.matchemphys.2021.124345

[164] Wei D, Tang QJ, Tong DG (2019) One-pot synthesis of $LiEuTiO_4$ as an anode material for lithium-ion batteries operating at 0.8 V. J Taiwan Inst Chem Eng 96:223–228. https://doi.org/10.1016/j.jtice.2018.11.014

[165] Hashemi E, Poursalehi R, Delavari H (2019) Formation mechanisms, structural and optical properties of Bi/Bi_2O_3 One dimensional nanostructures prepared via oriented aggregation of bismuth based nanoparticles synthesized by DC arc discharge in water. Mater Sci Semicond Process 89:51–58. https://doi.org/10.1016/j.mssp.2018.08.028

[166] Cui B, Hu B, Liu J et al (2018) Solution-plasma-assisted bimetallic oxide alloy nanoparticles of Pt and Pd embedded within two-dimensional $Ti_3C_2T_x$ nanosheets as highly active electrocatalysts for overall water splitting. ACS Appl Mater Interf 10:23858−23873. https://doi.org/10.1021/acsami.8b06568

[167] Islam Z, Watthanaphanit A, Chae S et al (2021) High electrical conductivity and oxidation reduction reaction activity of tungsten carbide/carbon nanocomposite synthesized from palm oil by solution plasma process. Mater Express 11:1587−1593. https://doi.org/10.1166/mex.2021.2035

[168] Niyitanga T, Jeong HK (2019) Hydrogen and oxygen evolution reactions of molybdenum disulfide synthesized by hydrothermal and plasma method. J Electroanal Chem 849:113383. https://doi.org/10.1016/j.jelechem.2019.113383

[169] Bratescu MA, Takai O, Saito N (2013) One-step synthesis of gold bimetallic nanoparticles with various metal-compositions. J Alloys Compounds 562:74–83. https://doi.org/10.1016/j.jallcom.2013.02.033

[170] Zhang J, Hu X, Yang B et al (2017) Novel synthesis of PtPd nanoparticles with good electrocatalytic activity and durability. J Alloys Comp 709:588–595. https://doi.org/10.1016/j.jallcom.2017.03.202

[171] Nominé AV, Tarasenka N, Nevar A et al (2022) Alloying nanoparticles by discharges in liquids: a quest for metastability. Plasma Phys Control Fusion 64:014003. https://doi.org/10.1088/1361-6587/ac35f0

[172] Sirotkin N, Khlyustova A (2022) The Oxide Nanostructures Formation Mechanisms in Underwater Plasma in Terms of Electrochemistry. Plasma Chem Plasma Process 42:1003–1013. https://doi.org/10.1007/s11090-022-10263-1

[173] Sirotkin N, Khlyustova A (2023) The Electrophysical Characteristics of Underwater Impulse Discharge Plasma in the Processes of Creating Multifunctional Composites. Plasma Chem Plasma Process 43:561–575. https://doi.org/10.1007/s11090-023-10329-8

[174] Yu F, Wang C, Li Y et al (2020) Enhanced solar photothermal catalysis over solution plasma activated TiO_2. Adv Sci 7:2000204. https://doi.org/10.1002/advs.202000204

[175] Ziashahabi A, Poursalehi R, Naseri N et al (2022) Shed light on defect induced enhanced visible-light photocatalysis activity of rutile TiO_2 nanoparticles: effects of annealing on blue-gray to light-gray transition. J Mater Res Technol 17:2400–2409. https://doi.org/10.1016/j.jmrt.2022.01.138

[176] Yu F, Wang C, Wang R et al (2023) Solution Plasma Engineering the Surface of Nitrogen Doped TiO_2 for Thermal-Assisted Photocatalysis. Available at SSRN: https://ssrn.com/abstract=4343353 or http://dx.doi.org/10.2139/ssrn.4343353

[177] Biazar N, Poursalehi R, Delavari H (2018) Optical and structural properties of carbon dots/TiO_2 nanostructures prepared via DC arc discharge in liquid. AIP Conf Proc 1920:020033. https://doi.org/10.1063/1.5018965

[178] Weerasinghe J, Li W, Zhou R et al (2020) Bactericidal silver nanoparticles by atmospheric pressure solution plasma processing. Nanomaterials 10:874. https://doi.org/10.3390/nano10050874

[179] Elwakil BH, Toderas M, El-Khatib M (2022) Arc discharge rapid synthesis of engineered copper oxides nano shapes with potent antibacterial activity against multi-drug resistant bacteria. Sci Rep 12:20209. https://doi.org/10.1038/s41598-022-24514-w

[180] Mohammadi M, Tavajjohi A, Ziashahabi A et al (2019) Toxicity, morphological and structural properties of chitosan-coated Bi_2O_3–$Bi(OH)_3$ nanoparticles prepared via DC arc discharge in liquid: a potential nanoparticle-based CT contrast agent. Micro Nano Lett 14(3):239–244. https://doi.org/10.1049/mnl.2018.5145

[181] Ko YB, Park YH, MubarakAli D et al (2023) Synthesis of antibacterial hydroxypropyl methylcellulose and silver nanoparticle biocomposites via solution plasma using silver electrodes. Carbohydr Polym 302:120341. https://doi.org/10.1016/j.carbpol.2022.120341

[182] Akarca G, Ozkan M, Ozcan T (2022) The impact of combination of solution plasma processing and pulsed electric field on the viability of probiotic bacteria microbial growth and structure of yoghurt drink. J Food Process Preserv 46:e16616. https://doi.org/10.1111/jfpp.16616